Solid Earth, 9, 1399–1419, 2018
https://doi.org/10.5194/se-9-1399-2018

Solid Earth Open Access EGU

Myrmekite and strain weakening in granitoid mylonites

Alberto Ceccato[1,a], **Luca Menegon**[2], **Giorgio Pennacchioni**[1], **and Luiz Fernando Grafulha Morales**[3]

[1]Department of Geosciences, University of Padova, 35131 Padova, Italy
[2]School of Geography, Earth and Environmental Sciences, University of Plymouth, PL48AA Plymouth, UK
[3]Scientific Centre for Optical and Electron Microscopy (ScopeM) – ETH Zürich, Zurich, Switzerland
[a]now at: School of Geography, Earth and Environmental Sciences, University of Plymouth, PL48AA Plymouth, UK

Correspondence: Alberto Ceccato (alberto.ceccato.2@phd.unipd.it)

Received: 19 July 2018 – Discussion started: 1 August 2018
Revised: 28 November 2018 – Accepted: 29 November 2018 – Published: 10 December 2018

Abstract. At mid-crustal conditions, deformation of feldspar is mainly accommodated by a combination of fracturing, dissolution–precipitation, and reaction-weakening mechanisms. In particular, K-feldspar is reaction-weakened by the formation of strain-induced myrmekite – a fine-grained symplectite of plagioclase and quartz. Here we use electron backscattered diffraction to (i) investigate the microstructure of a granodiorite mylonite, developed at $\sim 450\,^{\circ}C$ during cooling of the Rieserferner pluton (Eastern Alps); and (ii) assess the microstructural processes and the weakening associated with myrmekite development. Our analysis shows that the crystallographic orientation of plagioclase in pristine myrmekite was controlled by that of the replaced K-feldspar. Myrmekite nucleation resulted in both grain-size reduction and anti-clustered phase mixing by heterogeneous nucleation of quartz and plagioclase. The fine grain size of sheared myrmekite promoted grain-size-sensitive creep mechanisms including fluid-assisted grain boundary sliding in plagioclase, coupled with heterogeneous nucleation of quartz within creep cavitation pores. Flow laws, calculated for monomineralic quartz, feldspar, and quartz + plagioclase aggregates (sheared myrmekite) during deformation at $450\,^{\circ}C$, show that grain-size-sensitive creep in sheared myrmekite accommodated strain rates several orders of magnitude higher than monomineralic quartz layers deforming by dislocation creep. Therefore, diffusion creep and grain-size-sensitive processes contributed significantly to bulk rock weakening during mylonitization. Our results have implications for modelling the rheology of the felsic middle crust.

1 Introduction

Localization of ductile strain within rocks arises from weakening associated with grain-size refinement processes by dynamic recrystallization, metamorphic reactions, and microfracturing (e.g. Platt, 2015, and reference therein). Grain-size reduction, accompanied by phase mixing in polymineralic rocks at high strains, commonly results in a switch of deformation mechanism from grain-size-insensitive (GSI) to grain-size-sensitive (GSS) creep – one of the most effective strain-weakening mechanisms within shear zones (Kruse and Stünitz, 1999; Kilian et al., 2011; Menegon et al., 2013). Feldspars locally form the load-bearing framework of crustal rocks (Handy, 1994). At mid-crustal conditions, feldspar deformation mainly occurs by microfracturing and dissolution–precipitation processes, typically associated with metamorphic reactions (Behrmann and Mainprice, 1987; Michibayashi, 1996; Stünitz and Tullis, 2001; Gueydan et al., 2003; Ree al., 2005). Kfs (K-feldspar) is commonly replaced by myrmekite – a fine-grained symplectic aggregate of Qtz (quartz) and Plg (plagioclase) (Becke, 1908; Vernon, 1991). Myrmekite replacement is either related to Kfs chemical instability (Cesare et al., 2002), in some cases involving local metasomatic fluids (Phillips, 1980), or triggered by stress concentration and intra-crystalline strain in Kfs during deformation (Simpson and Wintsch, 1989; Menegon et al., 2006). This replacement is acknowledged as a weakening mechanism during ductile deformation of granitoid rocks (LaTour and Barnett, 1987; Simpson and Wintsch, 1989; MacCaffrey, 1994; O'Hara et al., 1997; Tsurumi et al., 2003; Pennacchioni, 2005; Menegon et al., 2006; Pennacchioni and Zucchi, 2013; De Toni et al., 2016). Deforma-

tion and shearing of myrmekite result in a fine-grained Plg + Qtz aggregate, which is manifestly weaker than original coarse Kfs (Tsurumi et al., 2003; Ree et al., 2005; Ciancaleoni and Marquer, 2006). In general, a fine grain size and the local presence of grain boundary aqueous fluid promote phase mixing and the development of ultramylonites (Vernon, 1991; Kilian et al., 2011; Czaplińska et al., 2015). Although the key role of myrmekite in strain localization has been recognized, it has not been accompanied with a quantitative analysis of the deformation mechanisms within myrmekite-derived, fine-grained Plg + Qtz aggregates.

Here we present a detailed analysis of myrmekite evolution, from the nucleation stage within Kfs to the development of sheared Plg + Qtz aggregates, and of the associated rheological weakening that resulted in strain localization in the mylonites of the Rieserferner granitoid pluton (Eastern Alps). In this pluton, ductile shear zones nucleated along joints that were locally filled with Qtz and Ep (epidote) veins during post-magmatic cooling (Ceccato et al., 2017; Ceccato and Pennacchioni, 2018). The progressive development of granodiorite mylonite was associated with consumption of Kfs by myrmekite leading to increasingly interconnected fine-grained Plg + Qtz layers. Microstructures of granodiorite mylonite have been analysed to characterize the following: (i) the process of myrmekite nucleation; (ii) the deformation mechanisms during myrmekite shearing and transition to Plg + Qtz aggregates; (iii) the deformation mechanisms of pure Qtz layers; and (v) the deformation mechanisms of Kfs porphyroclasts and of new Kfs grains during mylonitization. Furthermore, the application of mixed flow laws of the aforementioned deformation mechanisms for polymineralic aggregates allows for the degree of rheological weakening resulting from deformation of myrmekite to be quantified. The current paper represents a first attempt at quantitatively estimating, based on a robust microstructural analysis, the rheological effects of the development of myrmekite during mylonitization of granitoids, and at determining the deformation mechanisms in syn-kinematic monomineralic and polymineralic aggregates at mid-crustal conditions. This estimate was not attempted yet. This analysis is validated by comparison with experimental data on deformation of polyphase mixtures.

2 Geological setting and field description

The tonalitic–granodioritic Rieserferner pluton (Eastern Alps; Bellieni, 1978) was emplaced at $\sim$ 15 km depth (0.4 GPa; Cesare et al., 2010) into the Austroalpine nappe system at 32 Ma (Romer and Siegesmund, 2003). During post-magmatic cooling, a main set of ductile shear zones exploited shallowly ESE-dipping joints, and the joint-filling Qtz and Ep veins (set 2 of Ceccato and Pennacchioni, 2018). The temperature of ductile shearing has been estimated at 420–460 °C based on thermodynamic modelling (Ceccato, 2018). Ductile shearing along joints and Ep-filled joints resulted in centimetres-thick heterogeneous shear zones with a sigmoidal-shaped foliation in the host granodiorite (Ceccato and Pennacchioni, 2018) likely reflecting fluid–rock interaction at the vein selvages (Pennacchioni and Mancktelow, 2018). In contrast, Qtz veins filling the joints sharply localized homogeneous shearing (Ceccato et al., 2017).

In this study we analyse a sample of mylonitic shear zone within the Rieserferner granodiorite (sample ID: 10-019A; sample coordinates: 46°55′24.8″ N 12°07′36.2″ E). The structural mesoscale context of the studied sample is well illustrated by Ceccato and Pennacchioni (2018) and in particular by the map in Fig. 4 of their Supplement.

3 Analytical methods

Polished thin sections of granodiorite mylonite were prepared for the study of the microstructure and of the crystallographic preferred orientations (CPOs). The thin sections were made from rock chips cut parallel to the stretching lineation and perpendicular to the shear plane (XZ plane of finite strain ellipsoid).

Electron backscattered diffraction (EBSD) analysis was carried out on a JEOL 7001 FEG SEM equipped with a NordLys Max EBSD detector (AZTec acquisition software, Oxford Instruments) at the Electron Microscopy Centre of Plymouth University. EBSD patterns were acquired on rectangular grids with step sizes of 0.2, 0.3, and 0.35 µm. Working conditions during acquisition of EBSD patterns were 20 kV, 70° sample tilt, high vacuum, and a working distance between 17 and 23 mm. A detailed description of the EBSD post-processing methods and of the image analysis are reported in Appendix A. The microstructural and CPO analysis conducted with EBSD were complemented with cathodoluminescence (CL) and microchemical analyses.

CL imaging was performed in a FEI Quanta 200 FEI equipped with Gatan monocle detector. Imaging was performed using an accelerating voltage of 20 kV, beam current of 8 nA and a working distance of 20 mm in C-coated (15 nm) thin sections used for EBSD analysis. To avoid incorrect interpretation of potential artefacts in the sample, secondary electron and backscatter electron (BSE) images were collected simultaneously with CL.

Microchemical analyses were performed with wavelength-dispersive spectroscopy (WDS) at the Electron Microprobe Laboratory at the Università degli Studi di Milano with a Jeol 8200 Super Probe; the operating conditions were 15 kV accelerating voltage, 5 nA (Kfs and Plg) beam current. The Pouchou and Pichoir (PAP) correction programme was applied to convert X-ray counts into oxide weight percentages.

4 Microstructure

The Rieserferner granodiorite consists of Qtz, Plg, Kfs, Bt (biotite), Ep, Hbl (hornblende), Ap (apatite), and Ttn (titanite). The magmatic Plg displays normal oscillatory zoning (An_{58} – An_{32}). Plg crystals are arranged in glomeroclasts, included in Kfs ($Or_{93}Ab_7$). Various grain-size reduction mechanisms accompanied the development of a mylonitic foliation in the granodiorite: (i) recrystallization of Qtz and Bt (Fig. 1a, b), (ii) formation of myrmekite after Kfs (Fig. 1c, d), (iii) microfracturing of feldspar, and (iv) formation of Plg ($An_{29}Ab_{71}Or_{<1}$) + Ttn + Wmca (White Mica) symplectite at Bt–Plg boundaries (Pennacchioni et al., 2006; Johnson et al., 2008). Pristine myrmekite makes a transition to fine-grained aggregates of dominant Plg + Qtz extending into the foliation (Fig. 1b, e). The mylonitic foliation is defined by alternating layers of (i) monomineralic Qtz, (ii) Plg ($An_{26}Ab_{74}Or_{<1}$) + Qtz + Kfs, and (iii) Bt and recrystallized Bt/Plg (Fig. 1a). Syn-kinematic Kfs neoblasts ($Or_{96}Ab_4$) are found in strain shadows around porphyroclasts and dilatant fractures, and are in turn locally replaced by myrmekite (Fig. 1d). With increasing strain, the volume percentage of Kfs decreases from 19 % vol (undeformed rock and protomylonite) to 1 % vol–6 % vol (rare scattered porphyroclasts in mylonite and ultramylonite) (Fig. 2). As counterbalance, the volume percentage of fine-grained myrmekite and derived Plg + Qtz aggregates increases from 3 % vol (undeformed rock and protomylonite) to as much as 13 % vol (mylonite and ultramylonite) (Fig. 2). Ultramylonites consist of a fine-grained (ca. 10 µm grain size) well-mixed matrix of Qtz, Plg, Bt, Ep, Kfs, Ttn, Ap ± Grt (Garnet) ± Wmca.

5 EBSD and cathodoluminescence analysis

5.1 Pristine myrmekite

Pristine myrmekite shows (i) preferential development along grain boundaries of Kfs porphyroclast oriented parallel to the mylonitic foliation (Fig. 1b–e); (ii) lobate shape protruding into the Kfs (Fig. 1c); (iii) single grain structure of Plg within each lobe, embedding vermicular Qtz; (iv) rather constant spacing of Qtz vermicules of about 3–5 µm across the entire lobe (Fig. 1g); and (v) preferential elongation of the Qtz vermicules orthogonal to the myrmekite–Kfs boundary (Fig. 1g). The EBSD analysis shows that (i) Kfs and myrmekitic Plg commonly have similar crystallographic orientations ($(100)_{Kfs} \| (100)_{Plg}$, $(010)_{Kfs} \| (010)_{Plg}$, and $(001)_{Kfs} \| \| (001)_{Plg}$: Fig. 3b, c); (ii) Qtz vermicules do not share any crystallographic plane or direction with Kfs or myrmekitic Plg (Fig. 3b—d); (iii) Qtz vermicules do not show any obvious CPO, but they usually have similar crystallographic orientation within a myrmekite lobe (similar to what reported by Abart et al., 2014); and (iv) Dauphiné and Albite twins are occasionally observed in Qtz and Plg, respectively. The Plg of myrmekite lobes exhibits rare low-angle boundaries (misorientations $>2°$, $>5°$) that abut against the Qtz vermicules (Figs. 3e). The internal distortion of myrmekitic Plg is very small ($<1°$; Fig. S1a in the Supplement).

5.2 Sheared myrmekite: plagioclase + quartz aggregates

Plg + Qtz aggregates (± rare Kfs and Bt) wrap around Kfs porphyroclasts and are elongate into the foliation (Fig. 1e). These aggregates make transition to, and extend into the foliation from, pristine myrmekite and are hereafter referred to as sheared myrmekite.

Qtz grains in sheared myrmekite occur either as isolated single grains at triple and quadruple junctions between Plg grains or, less commonly, as polycrystalline aggregates elongated normal to the foliation (Fig. 4a). Qtz grains within sheared myrmekite have no CPO (Fig. 4b), show little internal distortion, and show rare low-angle boundaries with scattered misorientation axis distribution (Fig. 4c). Misorientation angle distribution for correlated pairs displays higher frequency than a random-pair distribution for misorientations $<15°$ and at 60° (Fig. 4d). The uncorrelated misorientation angle distribution approaches the random-pair distribution.

Plg grains do not show any obvious CPO (Fig. 4e), and display little internal distortion and rare low-angle boundaries. The low- and high-angle misorientation axes in crystal coordinate system are almost uniformly distributed (Fig. 4f). Even though very close to random-pair distribution, correlated misorientation distribution exhibits two distinct peaks at very low angles (<5–$10°$) and close to 180° (Fig. 4g). Misorientations $<70°$ occur with slightly higher frequency than the random-pair distribution. Albite twins and related 180° misorientations are rarely observed inside new grains (Figs. 3a–4a). In CL both myrmekitic Plg and Qtz have a grey shade similar to the surrounding non-myrmekitic Plg and Qtz (similar to Hopson and Ramseyer, 1990; Fig. 1f, h).

5.3 K-feldspar aggregates in strain shadows

In this section, EBSD data are used to describe the relationship between Kfs neoblasts and porphyroclasts. Kfs neoblasts occur in strain shadows around feldspar porphyroclasts, as well as dispersed within the sheared myrmekite (Fig. 3a, Area C in Figs. 4a; S2). In strain shadows, the orientation of (100) and (010) planes and [001] direction of the neoblasts is similar to that of the porphyroclast (Fig. 4h–j). In particular, the Kfs neoblasts show a CPO for (010) planes close to the *Y* kinematic axis (Fig. S2d), which is similar to the orientation of (010) in the adjacent porphyroclast. Misorientation axis-angle distributions show very few scattered data without any clear clustering (Fig. 4k). The grain size of new Kfs grains dispersed within sheared myrmekite is ca. 7 µm, comparable to that of the Plg in the surrounding

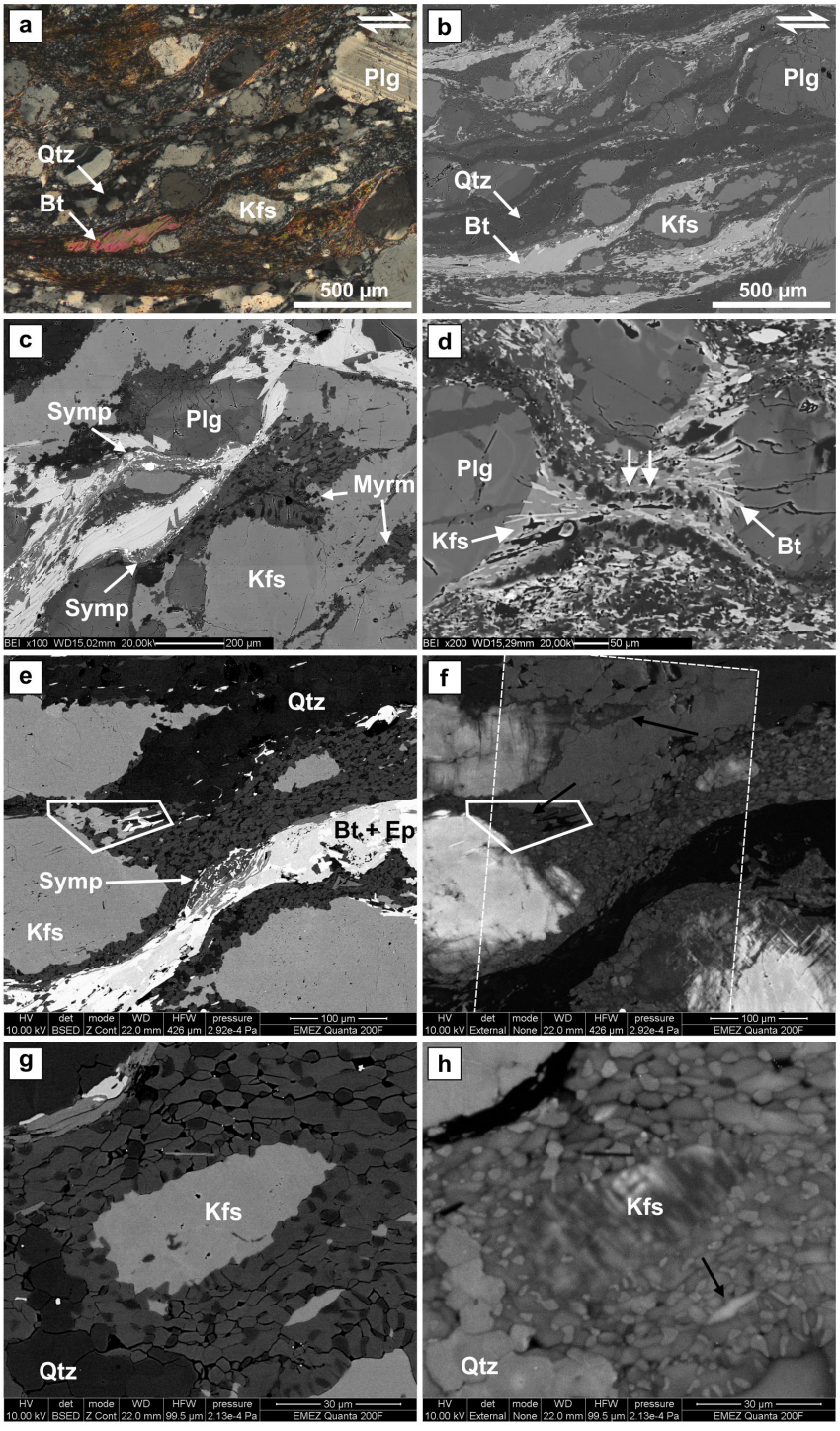

Figure 1. Microstructures of Rieserferner granodiorite mylonites. **(a)** Micrograph (crossed polarizers) showing the alternating layers of recrystallized Qtz, recrystallized Bt + Plg + Qtz, and Plg + Qtz. White arrows indicate layers of recrystallized Qtz (upper) and Bt (lower). **(b)** SEM-BSE image of the area shown in **(a)**. **(c)** SEM-BSE image of a pristine myrmekite (Myrm) replacing Kfs. Plg + Ttn symplectites (Symp) are indicated by white arrows. **(d)** SEM-BSE image of the Kfs + Bt tails in strain shadows between two Plg porphyroclasts. Kfs in the strain shadows is in turn replaced by myrmekite (white arrows). **(e)** SEM-BSE image of a Kfs porphyroclast and of sheared myrmekite. Pristine myrmekite developed on Kfs boundaries parallel to the mylonitic foliation are sheared to form Plg + Qtz aggregates (sheared myrmekite). The white polygon encloses Kfs neoblasts in strain shadows and sheared myrmekite. Plg + Ttn symplectites (Symp) are indicated by white arrows. **(f)** CL image of **(e)**. Black arrows indicate the Kfs in strain shadows and porphyroclast tails showing dark-grey homogeneous CL shades. Note the alteration of the CL signal in Qtz after the EBSD scan (area delimited by white dashed line). **(g)** Kfs and sheared myrmekite aggregate (particular of the EBSD map of Fig. 3). **(h)** CL image of **(g)**.

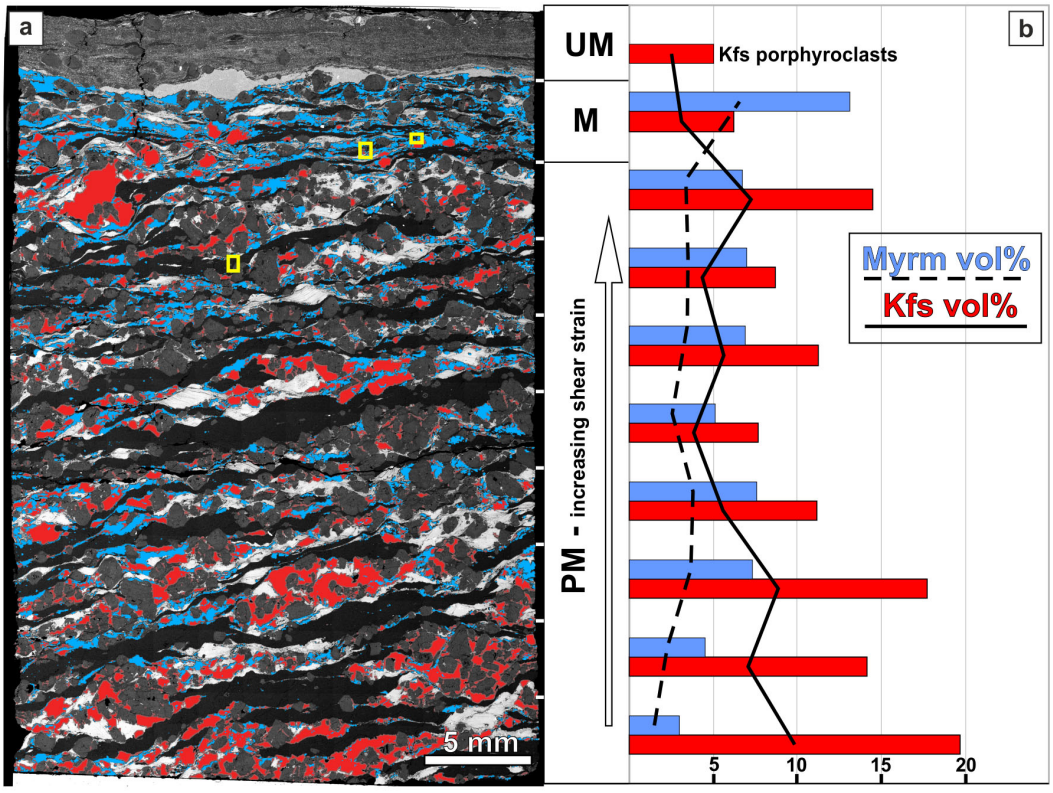

Figure 2. Phase distribution and abundance across a strain gradient in a granodiorite mylonite. **(a)** Mosaic of SEM-BSE images with the Kfs and the myrmekite + sheared myrmekite coloured in red and pale blue, respectively, and Qtz coloured in black. The yellow rectangles indicate the location of the EBSD maps of Figs. 3, 4, 5, and S2. **(b)** Bar diagram showing the volume amount of Kfs (red bars) and myrmekite (pale blue bars) across the microstructure: PM represents protomylonite; M represents mylonite; and UM represents ultramylonite.

sheared myrmekite (Fig. 5l). The CL imaging of Kfs highlights a complex microstructure, which is different between new grains and porphyroclasts. The porphyroclasts show a homogeneous bright shade overprinted by a complex pattern of dark-grey CL shade (indicated by black arrows in Fig. 3b, d, f). Kfs grains in sheared myrmekite and tails around porphyroclasts show a homogeneous dark-grey CL shade (indicated by black arrows in Fig. 1f–h). Kfs aggregates elongated parallel to the foliation and enveloped by sheared myrmekite are characterized by bright irregularly shaped Kfs cores (porphyroclasts) surrounded by dark-grey shaded Kfs.

5.4 Quartz layers along foliation

Monomineralic Qtz layers defining the mylonitic foliation (Figs. 2, 3, 4 and 5) show a variable grain size, and a shape preferred orientation (SPO) weakly inclined to the foliation consistently with the sense of shear. Dauphiné twin boundaries are widespread (red boundaries in Fig. 5a). The Qtz *c*-axis CPO defines an asymmetric Type-II girdle inclined at high angle to the local mylonitic foliation (Fig. 5b). The pole figures of *c* axis and $\langle a \rangle$ directions show maxima roughly aligned with the *Y* and the *X* kinematic directions, respectively. Misorientation axis distribution for low-angle misorientation ($< 10°$) exhibits a wide maximum close to *c* axis and $\langle \pi - \pi' \rangle$ directions in crystal coordinates. These misorientation axes preferentially cluster close to (but slightly offset from) the *Y* kinematic direction in sample coordinates (Fig. 5c). High-angle misorientation axis distributions do not show any clear systematic pattern, except for misorientations around 60°. Misorientation angle distribution (Fig. 5d) shows two peaks at very low-angle misorientations ($< 10°$) and around 60° for correlated misorientations. Uncorrelated misorientation angle distribution is close to the random-pair distribution. CPOs and misorientation data of coarser grains do not differ from those of finer grains. In CL images the Qtz layers display an overall homogeneous signature, with darker-grey shades close to inclusions and layer boundaries (central quartz layers in Fig. S3b).

6 Phase spatial distribution, grain size, and aspect ratio

The results of image analysis of EBSD phase maps indicate that pristine and sheared myrmekite have the same phase ratio with ca. 18 % vol of Qtz. We have analysed the phase spatial distribution of Plg and Qtz in both pristine and sheared

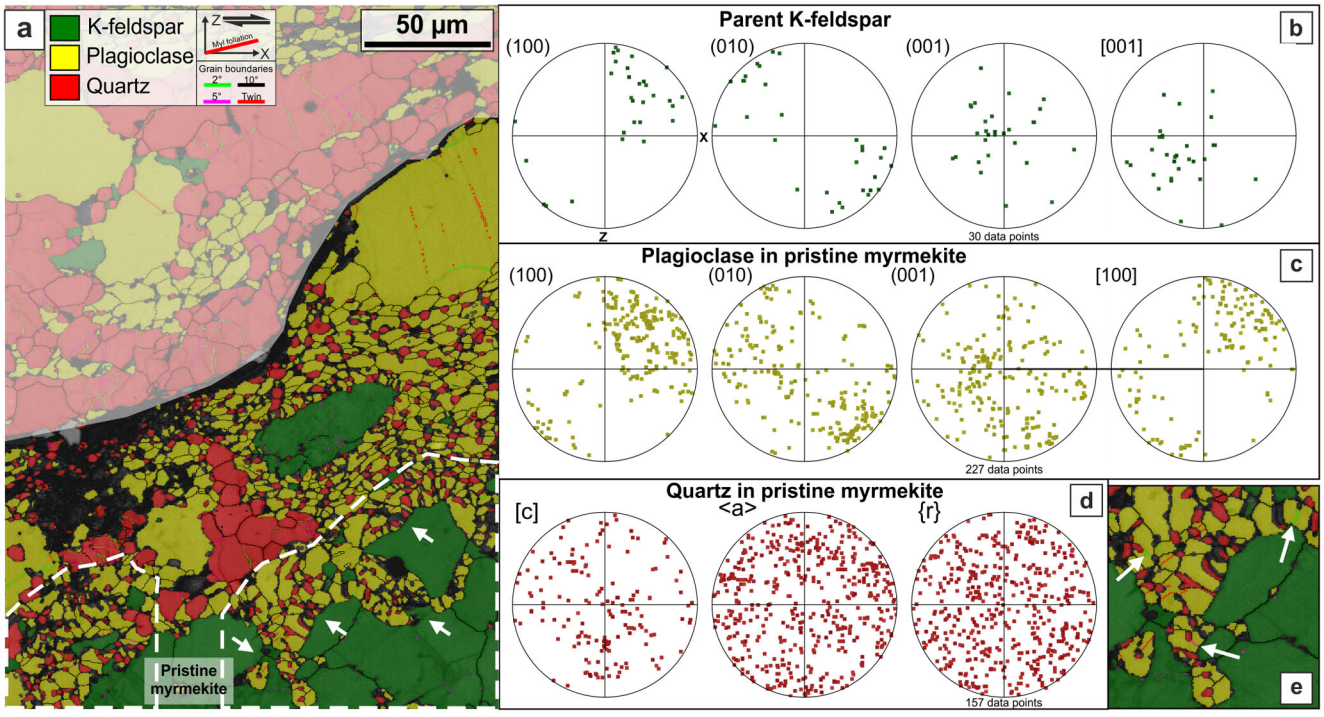

Figure 3. EBSD map and crystallographic orientation data of incipient myrmekite and parent Kfs. **(a)** EBSD-derived phase map. The area delimited by dashed polygons represents pristine myrmekite. Grain boundaries are colour-coded according to the maximum angle of misorientation observed across them. Pole figures for **(b)** Kfs grains on which pristine myrmekite nucleated; **(c)** Plg and **(d)** Qtz in pristine myrmekite. **(e)** Enlargement of EBSD map in **(a)** showing the low-angle (and twin, red) boundaries in plagioclase abutting against quartz vermicules (indicated by white arrows).

myrmekite to define their deviation from a random distribution, either towards a clustered or an anti-clustered distribution (Heilbronner and Barrett, 2014). Phase spatial distribution analysis of a two-phase aggregate compares the cumulative lengths of phase boundaries (boundaries between grains of a different phase) and of grain boundaries (boundaries between grains of the same phase) with those expected for a random distribution of the two phases. We have considered three types of boundaries: (i) Plg–Plg grain boundaries; (ii) Qtz–Qtz grain boundaries; and (iii) Plg–Qtz phase boundaries. The results (Fig. 6) show that, in pristine and sheared myrmekite (i) the surface area fraction of Qtz ranges between 0.55–0.75 and 0.55–0.65, respectively; (ii) Qtz–Qtz grain boundaries occur with a lower probability than for a random distribution, indicative of an anti-clustered distribution; (iii) Plg–Plg grain boundaries occur with a higher probability than for a random distribution indicative of a more clustered distribution; and (iv) Plg + Qtz aggregates display an anti-clustered distribution, with Plg–Qtz phase boundaries occurring with higher probability than for random distribution of phases. The results obtained from the analysis of the area shown in Fig. 6 are consistent with the results obtained from five other areas (not presented here for the sake of brevity).

Grain size distributions for Qtz (Fig. 7) and Plg (Fig. 8) are quite different for pristine myrmekite, sheared myrmekite, and in monomineralic Qtz layers. In pristine myrmekite, single large grains of Plg (20–50 µm, Fig. 8a) embed Qtz vermicules ~ 3 µm in equivalent diameter (Fig. 7a). In sheared myrmekite, Qtz grain size is around 3 µm (Area B in Figs. 4a; 7b), but locally increases to > 10 µm (Area C in Figs. 4a; 7c); individual Qtz grains show polygonal, equant shapes (aspect ratio, AR, of long to short axis; $1.5 < AR < 1.75$; Fig. 7e) or a weak SPO oriented at low angle to the local mylonitic foliation (Fig. 7e). Plg grains (average grain size of about 7 µm: Fig. 8b–c) are mainly polygonal and range in shape from almost equant to elongated ($1.75 < AR < 2$; Fig. 8d). Elongated grains define an SPO almost parallel to the local mylonitic foliation (Fig. 8d for Area B in Fig. 4a).

Monomineralic Qtz layers along the foliation show a variable grain size, usually ranging between 10 and 120 µm, mimicking a bimodal grain size distribution with maxima centred at 20–35 and 50–70 µm (Figs. 7d and S4). The coarser grain size (> 40 µm) is observed close to the centre of Qtz layers. These grains are usually characterized by subgrains ranging in size between 20 and 35 µm. The smaller grain size (< 40 µm) commonly envelopes the coarser grains, in addition to prevailing at the boundary between monomin-

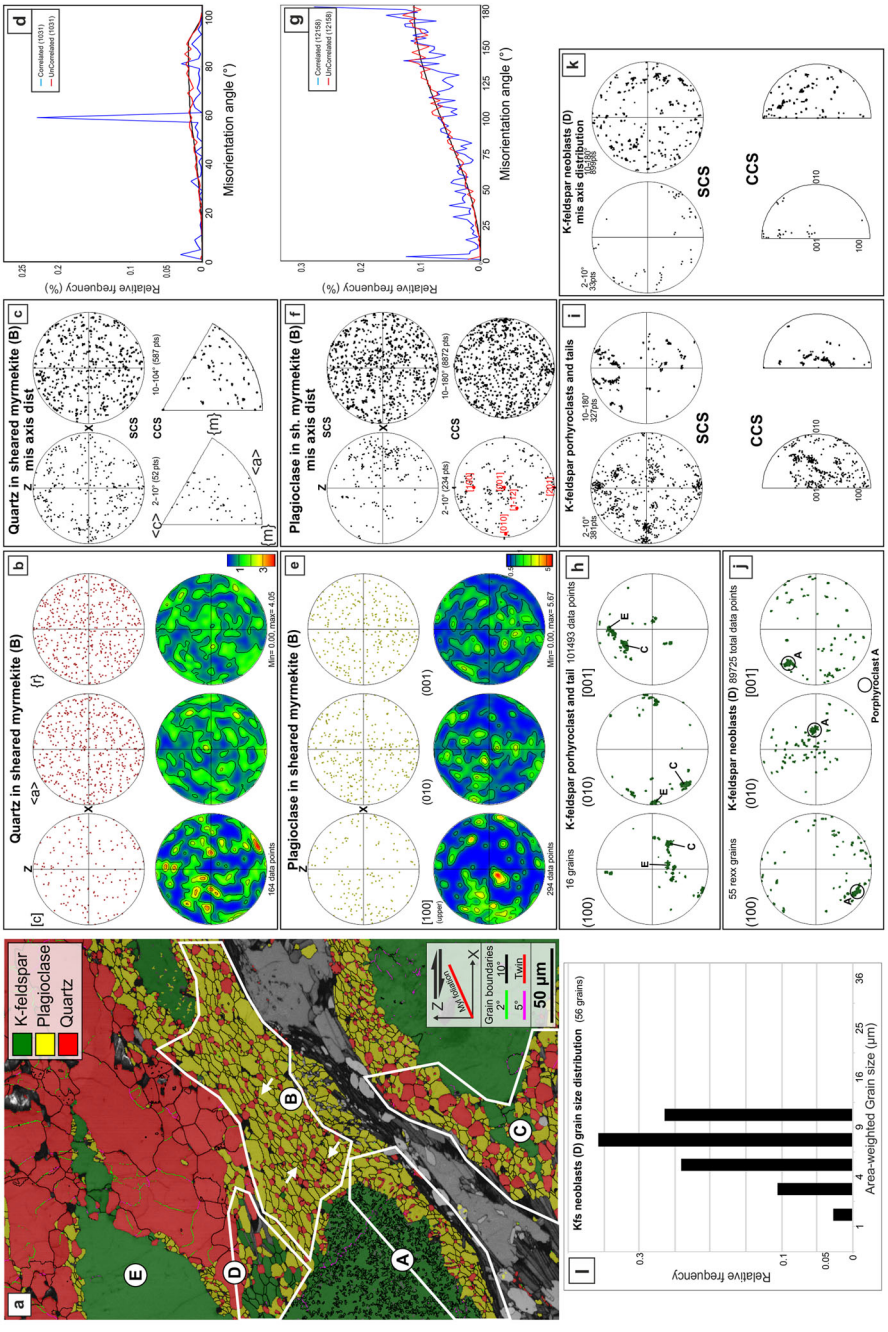

Figure 4. EBSD map and crystallographic orientation data of pristine and sheared myrmekite of Fig. 1e. **(a)** EBSD phase map including areas (A, B, C, D) selected for grain size analysis and phase distribution analysis. **(b)** Pole figures for Qtz from the sheared myrmekite of Area B. Upper row: scattered data. Lower row: contoured data. **(c)** Misorientation axis distributions for Qtz in sample (upper row) and crystal (lower row) coordinate system. **(d)** Misorientation angle distribution for Qtz. **(e)** Pole figures for Plg from sheared myrmekite of Area B. Upper row: scattered data. Lower row: contoured data. In this case, the [100] Plg pole figure is reported in upper hemisphere, where the maximum has been observed. **(f)** Misorientation axis distributions for Plg in sample (upper row) and crystal (lower row) coordinate system. **(g)** Misorientation angle distribution for Plg. **(h)** Pole figures of the crystallographic orientation of Kfs porphyroclasts included in Areas C and E and respective tails. **(i)** Misorientation axis distributions in sample (upper row) and crystal (lower row) coordinate system for porphyroclasts and tails. **(j)** Pole figures of the crystallographic orientation of Kfs porphyroclast A and Kfs neoblasts in the strain shadow (Area D). **(k)** Misorientation axis distributions in sample (upper row) and crystal (lower row) coordinate system for Kfs neoblasts. **(l)** Grain size distribution for the Kfs neoblasts.

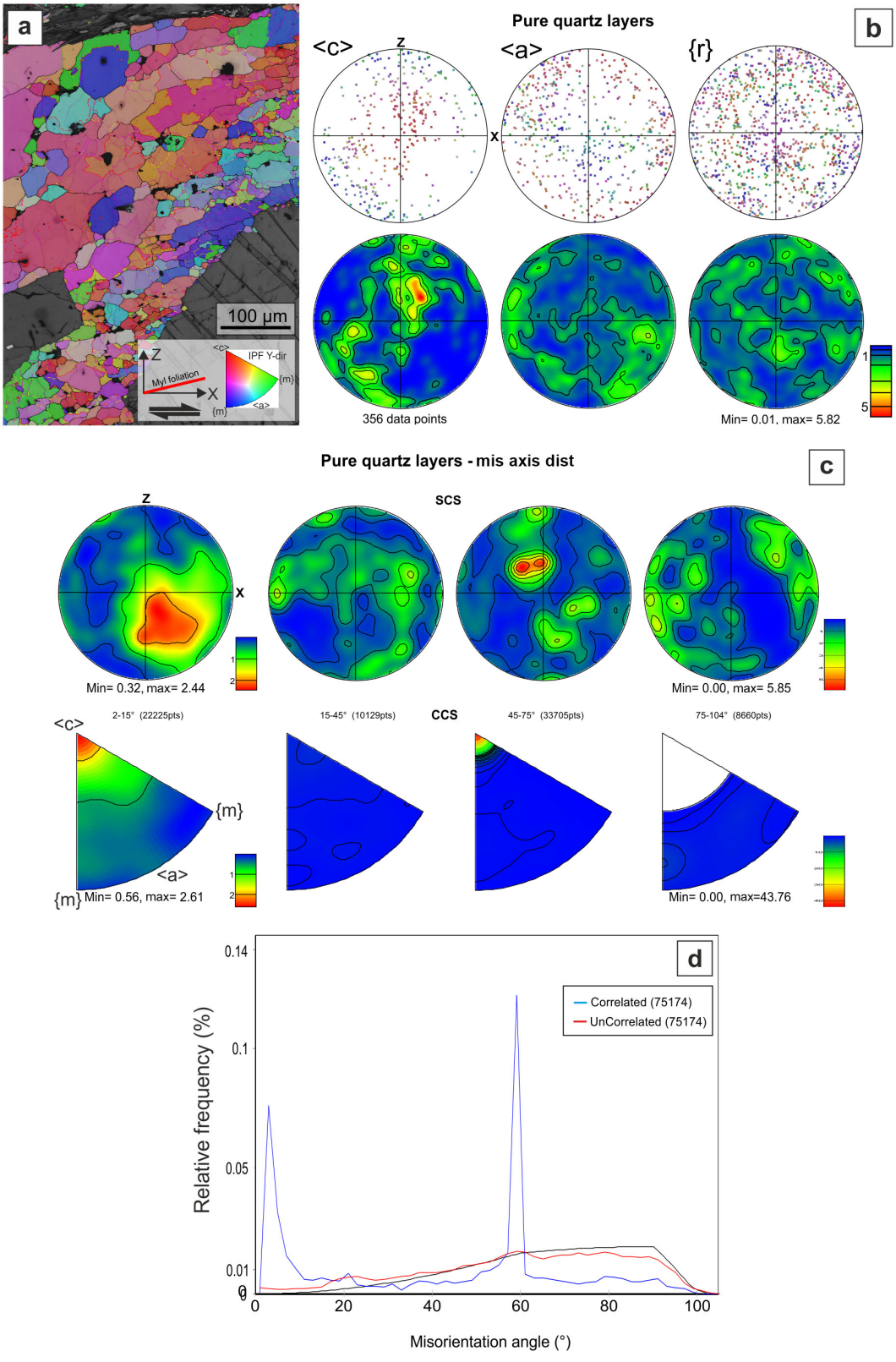

Figure 5. EBSD orientation data and mapping for pure Qtz layers. **(a)** Orientation map colour coded according to the inverse pole figure for Y direction reported in the lower right corner. **(b)** Area-weighted grain-size distribution for pure Qtz layer. **(b)** Pole figures for Qtz $[c]$, $\langle a \rangle$ and $\{r\}$ crystallographic elements. **(c)** Misorientation axis distributions in sample (upper row) and crystal (lower row) coordinate system. **(d)** Misorientation angle distribution for Qtz.

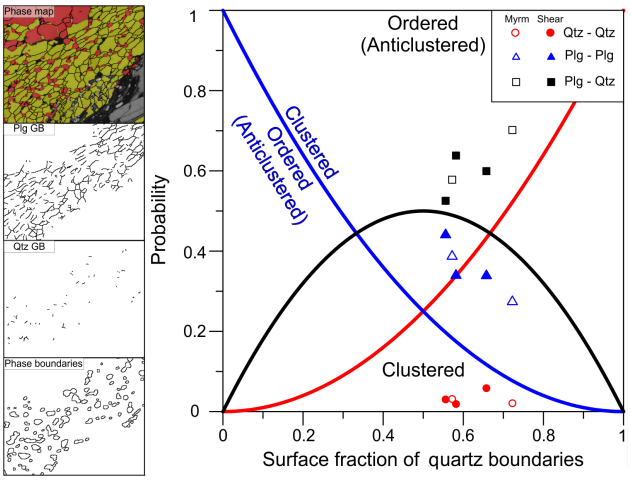

Figure 6. Image analysis of the phase spatial distribution in myrmekite. The diagram reports phase- and grain-boundary fractions in pristine and sheared myrmekite. Continuous curves represent the theoretical probability of phase- and grain-boundary fraction as a function of Qtz content expected for a random distribution in a two-phase aggregate. The small maps on the left-hand side report one of the analysed areas (Area C. Fig. 4), showing from the top to the bottom the phase map, the Plg grain boundaries, the Qtz grain boundaries, and the Plg–Qtz phase boundaries.

eralic Qtz layers and sheared myrmekite, or around feldspar porphyroclasts (Figs. 3, 4 and S4e).

7 The rheology of the Rieserferner mylonites

The rheological effect of transformation of coarse Kfs to fine-grained sheared myrmekite and the transition to an interconnected, weak, fine-grained microstructure (Handy, 1990) is estimated here by investigating the deformational behaviour of different mixtures of Plg and Qtz, in which deformation is accommodated either by dislocation creep or by diffusion creep. Our simplified model does not include Bt, Wmca or Bt + Plg aggregates. Based on the deformation mechanisms identified from the microstructural analysis, deformation mechanism maps have been calculated and plotted as grain size vs. differential stress and on differential stress vs. strain rate diagrams for the following three end-member compositions (Fig. 9):

i. monomineralic Qtz layer deforming via both dislocation and diffusion creep (Fig. 9a);

ii. sheared myrmekite, modelled as 80 % vol Plg (An_{60})+ 20 % vol Qtz deforming via both dislocation creep and GSS creep (Fig. 9b); the input grain size is 7 µm, identical for both minerals;

iii. a mixture of 60 % Plg (An_{100})+ 40 % Qtz assumed as a simplified composition representative of a mica-free granitoid rock deforming only by dislocation creep (after referred to as "granitoid", Fig. 9c).

The flow law of Hirth et al. (2001) has been used to calculate the dislocation creep component in deformation mechanisms maps for Qtz:

$$\dot{\varepsilon} = A_{\mathrm{q}} f_h \sigma^n e^{(-\frac{Q_q}{RT})}, \quad (1)$$

where A_{q} is the pre-exponential factor for Qtz ($\mathrm{MPa}^{-n}\,\mathrm{s}^{-1}$); f_h is the water fugacity; σ is the differential stress (MPa); n is the stress exponent; Q_q is the activation energy (J); R is the gas constant ($\mathrm{J\,K\,mol}^{-1}$); and T is the temperature (K). The contribution of diffusion creep in quartz is considered to come from pressure-solution creep and has been calculated using the flow law for thin-film pressure-solution creep of den Brok (1998):

$$\dot{\varepsilon}_{qps} = C_2 \frac{\rho_{\mathrm{f}}}{\rho_{\mathrm{s}}} \frac{\sigma}{d^3} \frac{VcD_w}{RT}, \quad (2)$$

where C_2 is a shape constant; ρ_{f} and ρ_{s} are the fluid and solid densities ($\mathrm{kg\,m}^{-3}$), respectively; d is the grain size (µm); V is the molar volume ($\mu\mathrm{m}^3\,\mathrm{mol}^{-1}$); c is the solubility of the solid in the fluid phase (molar fraction); and D_w is the diffusivity of the solid in the grain-boundary fluid film ($\mu\mathrm{m}^2\,\mathrm{s}^{-1}$). The flow laws for poly-mineralic aggregates (e.g. sheared myrmekite and mica-free granitoid) have been calculated following the approach of Dimanov and Dresen (2005) and Platt (2015). The method allows a poly-mineralic aggregate flow law to be constructed by considering the proportional contribution of the minerals in the aggregate. The resulting flow laws for the polymineralic aggregates can be derived for both a GSS and GSI rheology and are outlined in detail in the Supplement. In our calculations only quartz and feldspar are considered as minerals of the aggregates. For quartz the flow laws used are those above (Eqs. 1 and 2), while for feldspar, the flow laws of Rybacki et al. (2006) have been used to calculate the contribution of dislocation and diffusion creep, respectively:

$$\dot{\varepsilon}_{\mathrm{disl}} = A_{\mathrm{f}} f_h \sigma^n e^{\left(-\frac{Q_f + pV^{\mathrm{act}}}{RT}\right)}, \quad (3)$$

$$\dot{\varepsilon}_{\mathrm{diff}} = A_{\mathrm{f}} f_h \frac{\sigma^n}{d^m} e^{\left(-\frac{Q_f + pV^{\mathrm{act}}}{RT}\right)}, \quad (4)$$

where $\dot{\varepsilon}_{\mathrm{disl}}$ represents the strain rate component given by dislocation creep; $\dot{\varepsilon}_{\mathrm{diff}}$ represents the strain rate component given by diffusion creep; A_{f} is the pre-exponential factor for feldspar ($\mathrm{MPa}^{-n}\,\mu\mathrm{m}^m\,\mathrm{s}^{-1}$); d is the grain size (µm); m is the grain-size exponent; p is the confining pressure (MPa); and V^{act} is the activation volume ($\mathrm{m}^3\,\mathrm{mol}^{-1}$). Flow law parameters are listed in Table 1. Details on the derivation of the deformation mechanism maps and on the calculation of the flow laws are given in the Supplement. The

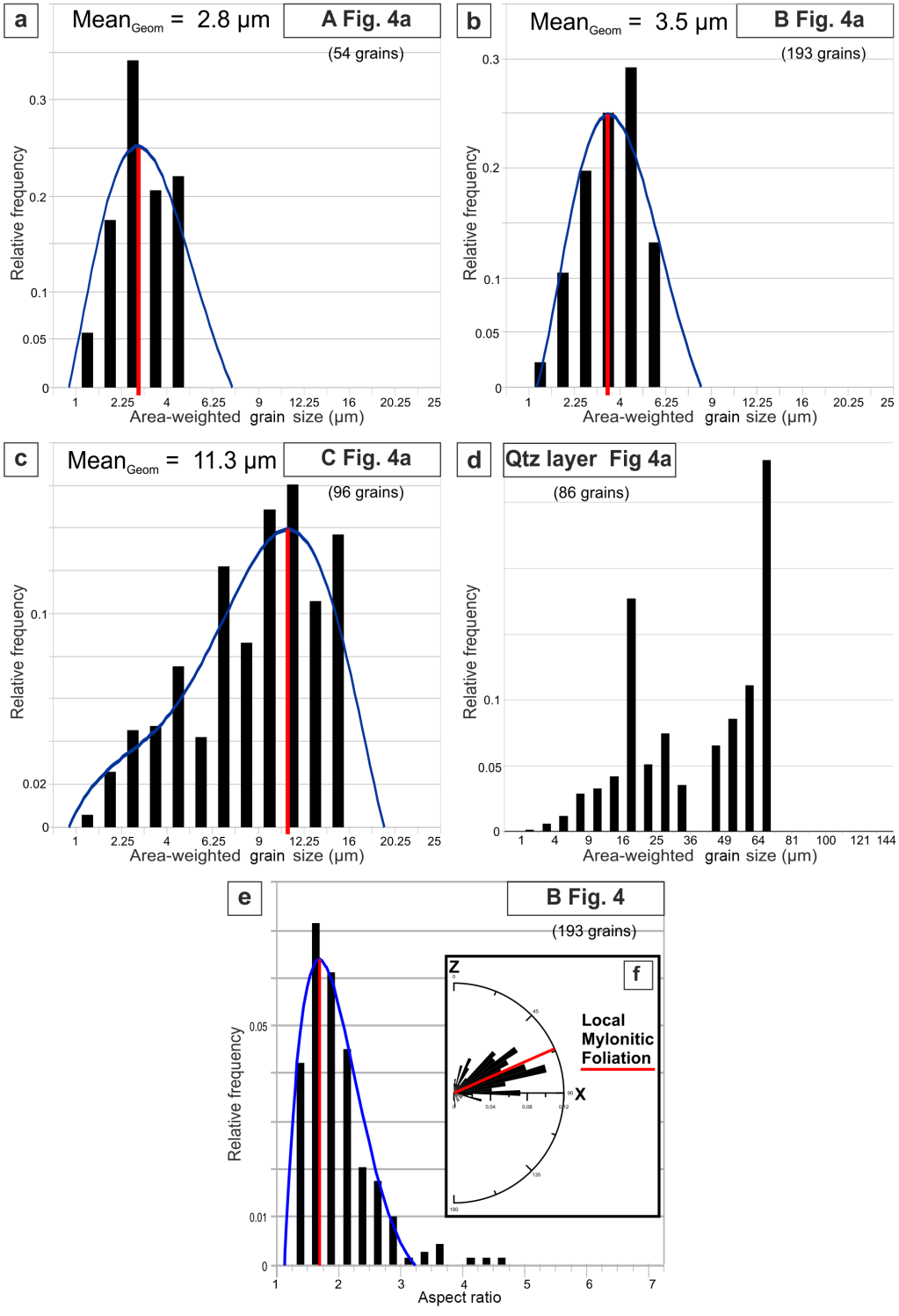

Figure 7. Area-weighted grain size distributions and SPO for Qtz. **(a)** Grain-size distribution for Qtz in incipient myrmekite A in Fig. 4a. **(b)** Grain size distribution for Qtz in sheared myrmekite B in Fig. 4a. **(c)** Grain-size distribution for Qtz in sheared myrmekite C in Fig. 4a. **(d)** Grain-size distribution for Qtz in monomineralic layer in Fig. 4a. **(e)** Relative frequency distribution of grain aspect ratio for Qtz. **(f)** Rose diagram showing the orientation of major axis of Qtz grains, defining a weak SPO. The distribution curve (blue line in grain size distribution diagrams) was obtained by interpolating distribution data with a sixth-degree polynomial equation in MS Office Excel. Relative frequencies are normalized to 1.

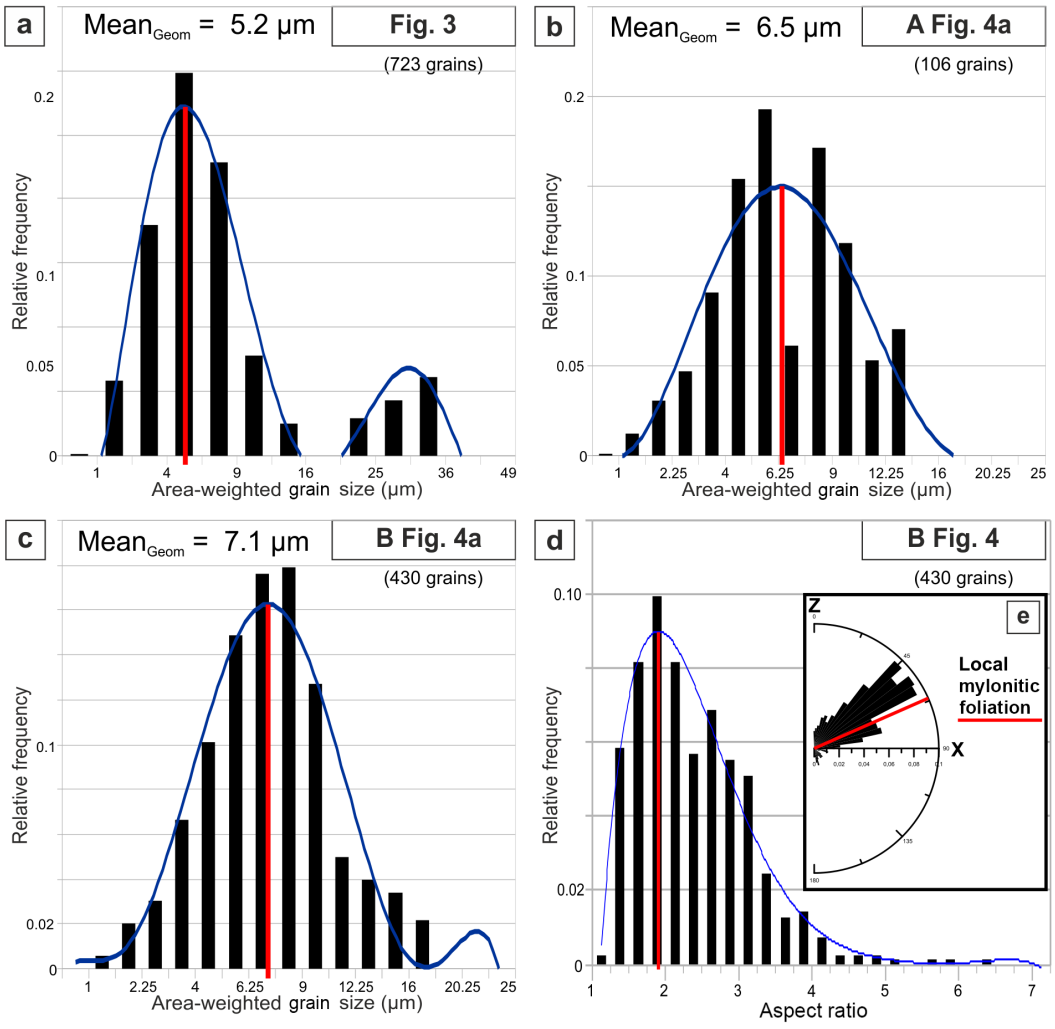

Figure 8. Area-weighted grain-size distributions and SPO for Plg. **(a)** Grain-size distribution for Plg in myrmekite of Fig. 3. **(b)** Grain-size distribution for Plg in incipient myrmekite A in Fig. 4a. **(c)** Grain-size distribution for Plg in sheared myrmekite B in Fig. 4a. **(d)** Relative frequency distribution of grain aspect ratio for Plg. **(e)** Rose diagram showing the orientation of major axis of Plg grains, defining a weak SPO. The distribution curve (blue line in grain-size distribution diagrams) was obtained by interpolating distribution data with a sixth-degree polynomial equation in MS Office Excel. Relative frequencies are normalized to 1.

model approximates the Reuss (iso-strain) conditions (Dimanov and Dresen, 2005). The flow laws and flow-law parameters were estimated for the pressure–temperature conditions of mylonitization of the Rieserferner (450 °C and 0.35 GPa; Ceccato, 2018). At these conditions, the calculated water fugacity is $f_h = 97$ MPa (Pitzer and Sterner, 1994). Fluid density, Qtz solubility, and diffusivity in the thin-film (grain boundary) fluid has been calculated following Fournier and Potter (1982) and Burnham et al. (1969). The flow-law parameters defined for An_{100} and An_{60} by Rybacki and Dresen (2004) have been adopted for our calculations to simulate different compositions of "granitoid" and myrmekitic feldspars. These are "wet" flow-law parameters that have been derived experimentally from deformation of fine-grained aggregates of An_{100} and An_{60} containing 0.004 wt % and 0.3 wt % of water, respectively. In our calculations, all the Kfs has been considered as Plg, given the lack of flow-law parameters for Kfs (see discussion in Platt, 2015; Viegas et al., 2016). Our calculation includes the contribution of grain boundary sliding (GBS) to the bulk strain rate of the feldspar aggregate, which is considered in the flow-law parameters adopted here (see discussions in Xiao et al., 2002; Rybacki and Dresen, 2004).

The grain size vs. differential stress and differential stress vs. strain rate diagrams in Fig. 9 suggest the occurrence of different rheological behaviours that can be interpreted in terms of strain partitioning between aggregates with different "compositions". The results indicate that the three considered types of aggregates can be ranked, from the strongest to the weakest, as follows: (i) Qtz-feldspar "granitoid" ag-

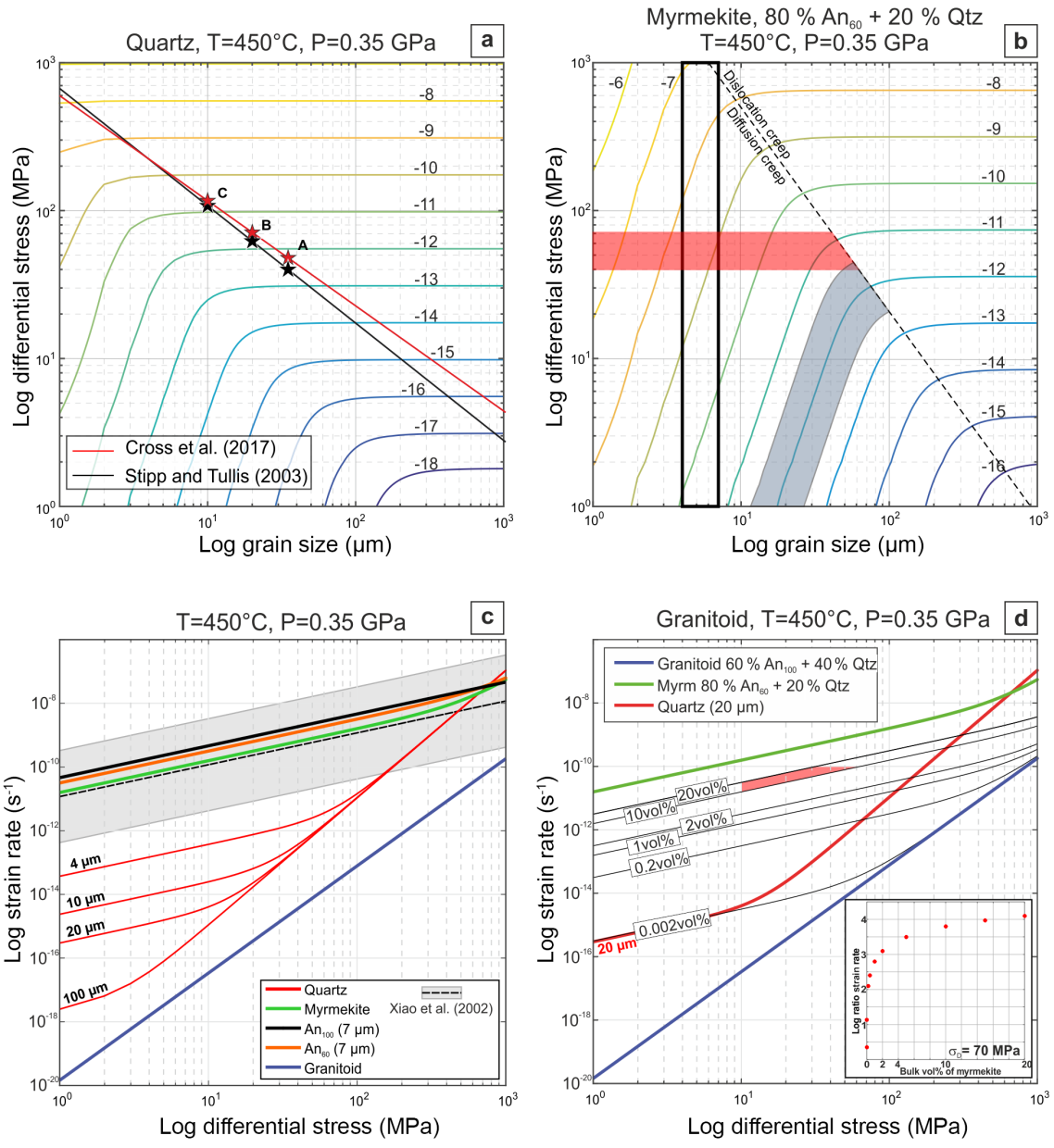

Figure 9. Diagrams derived from the calculation of the rheological model explained in the text. Grain size vs. differential stress map with contoured strain rate curves calculated for **(a)** Qtz and **(b)** 80 % Plg (An_{60})+ 20% Qtz aggregates. **(a)** The piezometric curve from Stipp and Tullis (2003, black curve) and Cross et al. (2017, red curve) are reported. Red and black stars mark the differential stress/strain-rate conditions defined by the grain size observed in pure Qtz layers: **(a)** 35 µm; **(b)** 20 µm; **(c)** 10 µm (Ceccato et al., 2017). **(b)** The black dashed line represents the boundary between dislocation and diffusion creep dominated conditions. The black rectangle represents the grain size range (4–7 µm) observed in the sheared myrmekite. The grey semi-transparent polygon defines the field of possible grain-size and differential stress conditions for iso-strain-rate conditions defined from piezometric relations. **(c)** Log differential stress vs. log strain rate diagram reporting the curve calculated for pure Qtz with different grain sizes (4, 10, 20, 100 µm), sheared myrmekite, ideal granitoid rock and the curves representing the rheology of pure feldspar aggregates. For comparison, one of the curve obtained from experimental data of Xiao et al. (2002) is reported (black dashed curve). Grey field represents the uncertainties in the experimentally defined rheological curve. **(d)** Log differential stress vs. log strain rate diagram reporting the curve calculated for pure Qtz, sheared myrmekite, and ideal granitoid rock and the curves representing the rheology of a granitoid (60 % An_{100} Plg+ 40 % Qtz) with a variable amount of sheared myrmekite (80 % An_{60} Plg + 20 % Qtz). Maximum replacement is limited to 20 % of initial feldspar (see text for explanation). Transparent red polygon defines the stress-strain rate conditions for 15 % vol substitution of myrmekite (see text for explanation). The small figure inset shows the logarithm of the ratio between the strain rate of an ideal granitoid rock vs. that of a granitoid with increasing myrmekite substitution at the differential stress of 70 MPa.

Table 1. Parameters adopted in the rheological calculations. **(a)** List of the general parameters adopted in the rheological calculations. **(b)** Values of flow-law parameters adopted in the rheological calculations according to mineral phase and deformation mechanism.

(a)	Description	Value	Units	Reference
P	Pressure	350	MPa	4
T	Temperature	723	K	4
f_h	Water fugacity	97	MPa	5
R	Gas constant	8.314	$\mathrm{J\,K^{-1}\,mol^{-1}}$	
d	Grain size		µm	
n	Stress exponent			1, 2
m	Grain size exponent			1, 2
A	Pre-exponential factor		$\mathrm{MPa^{-n}\,\mu m^{m}\,s^{-1}}$	1, 2
Q	Activation energy		J	1, 2
ρ_f	Fluid density	837.5	$\mathrm{kg\,m^{-3}}$	
ρ_s	Solid density	2650	$\mathrm{kg\,m^{-3}}$	
C_2	Shape constant	44		3
V	Molar volume of quartz	22 690 000	$\mathrm{\mu m^3\,mol^{-1}}$	
c	Solubility of solid in the fluid phase	0.0014	molar fraction	6
D_w	Diffusivity of the solid in the grain-boundary fluid film	1.604×10^{-11}	$\mathrm{\mu m^2\,s^{-1}}$	3
V^{act}	Activation volume	0.00038	$\mathrm{m^3\,mol^{-1}}$	7
μ	Viscosity		$\mathrm{MPa\,s^{-1}}$	

(b)	Dislocation creep			Diffusion creep		
Phase	Quartz	Plagioclase		Quartz	Plagioclase	
Composition		An_{100}	An_{60}		An_{100}	An_{60}
n	4	3	3	1	1	1
m	0	0	0	3	3	3
A	6.30957×10^{-12}	398.1	0.031		50.1	12.6
Q	135 000	345 000	235 000	137 000	159 000	153 000
Reference	1	2	2	3	2	2

References: (1) Hirth et al. (2001). (2) Rybacki and Dresen (2004). (3) den Brok (1998). (4) Ceccato (2018). (5) Pitzer and Sterner (1994). (6) Fournier and Potter (1982). (7) Rybacki et al. (2006).

gregate; (ii) monomineralic Qtz aggregates; and (iii) sheared myrmekite. This ranking is validated by several field and microstructural observations, which highlight the strain localization capability of monomineralic Qtz layers (i.e. Qtz veins) and two-phase microstructural domains (i.e. sheared myrmekite) in granitoid rocks (Pennacchioni, 2005; Pennacchioni and Mancktelow, 2007; Pennacchioni and Zucchi, 2013; Pennacchioni et al., 2010; Menegon and Pennacchioni, 2010; Ceccato et al., 2017). The results of rheological calculation of Plg + Qtz aggregates deforming via diffusion creep (sheared myrmekite) are consistent and comparable with some of the experimental results of Xiao et al. (2002) extrapolated to natural geological conditions (Fig. 9c). The experimental data that best fit our estimated rheological curve are those obtained from triaxial deformation experiments of synthetic very fine-grained wet aggregate of 80 % vol An_{100} Plg (6 µm) +20 % vol Qtz (10 µm).

8 Discussion

The following discussion is structured in two main parts: firstly, the microstructural processes controlling nucleation and the deformation mechanisms during myrmekite shearing are discussed; then, the results of rheological calculation are discussed in the light of the previously identified deformation mechanisms in order to give a quantitative estimate of the rheological effects associated with the activity of different deformation mechanisms in mono- and polymineralic domains.

8.1 Formation and shearing of myrmekite

In the following sections, EBSD data presented earlier are discussed in order to gain new insights into the myrmekite nucleation process in the light of previously published works. The possible mechanisms involved during the transition from pristine to sheared myrmekite are then addressed, comparing the evolution of myrmekite to that of similar symplectites during shearing. Then, deformation mechanisms during

shearing of myrmekite are finally identified based on microstructures and EBSD data.

8.1.1 Crystallographic relationship between K-feldspar and myrmekitic phases

The EBSD analysis indicates that the Kfs and the overgrowing myrmekitic Plg have a similar crystallographic orientation, although with some scattering (Fig. 3b; Wirth and Voll, 1987). This suggests the occurrence of a topotactic replacive process where $(100)_{Kfs} \| (100)_{Plg}$, $(010)_{Kfs} \| (010)_{Plg}$, and $(001)_{Kfs} \| (001)_{Plg}$. The scatter in crystallographic orientation between Kfs and myrmekitic Plg is interpreted to result from deformation during and after myrmekite formation (see Sect. 8.1.2). The crystallographic orientation of myrmekitic Plg and Qtz was not controlled by neighbour Plg or Qtz grains previously in contact with the Kfs, unlike what is reported by other authors (Stel and Breedveld, 1990; Abart et al., 2014). As observed by Abart et al. (2014), the different myrmekite Qtz vermicules have a similar crystallographic orientation. The anti-clustered phase spatial distribution of pristine myrmekite is related to the process of heterogeneous phase nucleation during myrmekite formation (Wirth and Voll, 1987).

8.1.2 Transition from pristine to sheared myrmekite (plagioclase + quartz aggregates)

The sheared Plg + Qtz aggregates, wrapping Kfs porphyroclasts and elongated into the foliation, resulted from shearing of pristine myrmekite. The transition from pristine to sheared myrmekite was a dynamic process and here we try to constrain the processes involved as inferred from microstructural changes. These microstructural changes included (i) randomization of Plg CPO observed in pristine myrmekite; (ii) evolution of Plg grain size distribution from heterogeneous (ranging between 3 and 50 µm) in pristine myrmekite, to homogeneous and centred at 7 µm in sheared myrmekite (Figs. 3, 4 and 8a); (iii) coarsening of Qtz grains from < 3 µm thick vermicules to rounded-to-polygonal grains as large as 10 µm in sheared myrmekite (Fig. 7). The processes of grain-size evolution are probably related to the minimization of interfacial energy in the vermicular microstructure of pristine myrmekite (e.g. Odashima et al., 2007; Dégi et al., 2010). Qtz grain coarsening reflects annealing of the pristine vermicular microstructure after the reaction front moved further into the Kfs (Fig. 3a), and was probably aided by dissolution–precipitation processes. Qtz coarsening implies simultaneous grain-size refinement of Plg, which probably involved microfracturing with the development of local micro-cracks in myrmekitic Plg. Misorientation analysis on the few low and high misorientation angle boundaries inside pristine myrmekite (inside myrmekitic Plg) shows abrupt misorientations of as much as 8° across such boundaries, which could be interpreted as either micro-cracks or growth features considering the low internal distortion of grains (Figs. 3, S1). Microfractures could have originated from stress concentrations within the 3-D geometrically or mechanically composite structure of myrmekite (see Fig. 2 of Hopson and Ramseyer, 1990; Dell'Angelo and Tullis, 1996; Xiao et al., 2002). Therefore, the Plg grain size in the incipiently sheared aggregate may be controlled by the spacing between Qtz vermicules in pristine myrmekite. Myrmekite was then sheared along the mylonitic foliation from the contractional sites around the Kfs porphyroclast. Then, interconnected layers of sheared myrmekite developed from foliation-parallel stretching of isolated myrmekite mantling Kfs during mylonitization (similar to Boullier and Gueguen, 1975).

8.2 Deformation mechanisms in the Rieserferner mylonites

8.2.1 Sheared myrmekite

The microstructures of sheared myrmekite are consistent with GSS creep, including fluid-assisted GBS (Boullier and Gueguen, 1975; White, 1977; Stünitz and Fitz Gerald, 1993; Fliervoet et al., 1997; Jiang et al., 2000; Wheeler et al., 2001; Lapworth et al., 2002; Bestmann and Prior, 2003; Kilian et al., 2011; Menegon et al., 2013). Plg and Qtz of sheared myrmekite both display (i) a weak CPO; (ii) rare low-angle boundaries without systematic pattern of misorientation axis distribution; and (iii) correlated and uncorrelated misorientation angle distributions close to the theoretical random-pair distribution. All these features suggest very limited dislocation creep in both minerals (Kruse et al., 2001; Okudaira and Shigematsu, 2012; Miranda et al., 2016). In addition, sheared myrmekite show (i) fine-grained Plg and Qtz with polygonal, equant to slightly elongated shape (AR < 2); (ii) aligned grain boundaries (over the scale of several grain diameters) and common triple and quadruple junctions; and (iii) anti-clustered spatial distribution of Plg and Qtz.

Phase spatial distribution in deformed bimodal aggregates in mylonites is interpreted to reflect the activity of specific deformation mechanisms (Kruse and Stünitz, 1999; Menegon et al., 2013). In particular, diffusion creep in polymineralic aggregates is commonly accompanied by heterogeneous phase nucleation that promotes phase mixing and a high degree of anti-clustering in phase distribution (Kilian et al., 2011; Menegon et al., 2013). The occurrence of Qtz in triple and quadruple junctions and Qtz aggregates elongated orthogonal to the foliation in sheared myrmekite suggests creep cavitation and heterogeneous Qtz nucleation during GSS creep of Plg (Fusseis et al., 2009; Herwegh et al., 2011; Kilian et al., 2011). Heterogeneous phase nucleation in creep cavities led to the anti-clustered phase spatial distribution (Fig. 6; Hiraga et al., 2013; Menegon et al., 2015). The constant Plg grain size of sheared myrmekite may then result from the combination of initial spacing between Qtz vermicules in pristine myrmekite, diffusion creep processes,

and second-phase grain-boundary pinning during shearing (Herwegh et al., 2011). GSS processes, phase mixing and second-phase grain-boundary pinning, inhibit grain growth and stabilizes grain size, hindering the efficiency of dynamic recrystallization processes and self-sustaining the activity of GSS processes.

8.2.2 K-feldspar tails and neoblasts

Kfs is abundant in the low-strain portions of the mylonite (Fig. 2). Kfs porphyroclasts and tails do not show any CPO or misorientation axis distribution referable to dislocation creep processes (Figs. 4i, S2; Menegon et al., 2008, and reference therein). The similar crystallographic orientation between feldspar(s) porphyroclasts and either Kfs tails or fine neoblast aggregates can be explained by invoking epitaxial nucleation and growth during dissolution–precipitation (Figs. 4, S2). Dissolution–precipitation would be consistent with the Kfs aggregate microstructure observed under CL, which probably reflect either the different chemistry or the different intra-granular strain observed between magmatic ($Or_{93}Ab_7$) and synkinematic Kfs ($Or_{96}Ab_4$) (Shimamoto et al., 1991; Ramseyer et al., 1992; Götze et al., 1999; Słaby et al., 2008, 2014). The modification of the inherited CPO in fine-grained aggregates could be then related to the occurrence of anisotropic dissolution–precipitation processes and grain boundary sliding during myrmekite shearing (Behrmann and Mainprice, 1987; Menegon et al., 2008, 2013).

8.2.3 Monomineralic quartz layers

The microstructures, CL signatures, and CPO of monomineralic Qtz layers indicate deformation by dominant dislocation creep aided by sub-grain rotation (SGR) recrystallization (e.g. Fliervoet et al., 1997; Wheeler et al., 2001; Stipp et al., 2002; Bestmann and Pennacchioni, 2015). The misorientation axes distributions suggest the preferential activation of $\{m\}\langle a\rangle$ and $\{r-z\}\langle a\rangle$ slip systems (e.g. Ceccato et al., 2017, and references therein). The analysis of the grain orientation spread (GOS), to distinguish different generation of relict and/or recrystallized grains (Cross et al., 2017), suggests that there are no meaningful correlations between grain size and average grain distortion. This missing correlation may reflect a non-steady-state Qtz microstructure during a prolonged deformation history or, more likely, the development of the microstructures at different temperature conditions during pluton cooling. The bimodal grain size of recrystallized Qtz includes coarser grains that we infer developed during the relatively high-temperature bulk solid-state deformation of the host granodiorite predating the development of localized shear zones at 450 °C dominated by SGR recrystallization (Ceccato et al., 2017; Ceccato and Pennacchioni, 2018). Coarser grains in Qtz layers (grain sizes from $>40\,\mu m$) record differential stresses <40 MPa and strain rates of 10^{-13}–$10^{-14}\,s^{-1}$ as retrieved by applying the grain size paleopiezometer of Cross et al. (2017). Sub-grain and finer grains (20–35 µm in diameter) suggest that localized deformation and shearing occurred at differential stresses close to 40–70 MPa and strain rates of 10^{-11}–$10^{-12}\,s^{-1}$ (Stipp and Tullis, 2003; Cross et al., 2017).

8.3 The effect of myrmekite on strain localization

In the following, the results of rheological calculations are discussed in terms of their implications on strain localization in granitoid rocks. Firstly, we will address the different rheology and strain partitioning at the microstructural scale, considering the calculated rheology for the different mono- and poly-mineralic layers. Then, the effect of increasing myrmekite substitution on the bulk rheology of a granitoid rock is addressed, comparing the rheology of the simplified granitoid rock to that of a granitoid rock with increasing myrmekite substitution.

Our results show that in the Rieserferner mylonites an effective strength contrast between mono- and poly-mineralic layers occurs at the scale of the thin section as a consequence of the different deformation mechanisms. To quantify the effective strength contrast between the modelled layer compositions, we consider two end-member conditions: constant stress and constant strain rate. Assuming that the differential stress of 40–70 MPa, estimated from the finer grain size of Qtz (from 20 to 35 µm), is representative of the bulk flow stress of the mylonite, the Qtz aggregates deforming by dislocation creep (Fig. 9a) would flow at a strain rate of 10^{-11}–$10^{-13}\,s^{-1}$, whereas sheared myrmekite deforming via diffusion creep would flow at strain rates faster than $10^{-12}\,s^{-1}$, depending on the actual grain size of the aggregate (red transparent area in Fig. 9b). For the grain size range of sheared myrmekite (4–7 µm), the observed strain rates are always faster than $10^{-11}\,s^{-1}$, and for the above-defined differential stress range the calculated strain rate is of the order of $10^{-9}\,s^{-1}$ (intersection between red transparent area and black box in Fig. 9b). Therefore, assuming constant differential stress conditions, a strain-rate partitioning of 2–4 orders of magnitude is expected between monomineralic Qtz and sheared myrmekite (similarly to Behrmann and Mainprice, 1987). Assuming constant strain rate conditions of 10^{-11}–$10^{-12}\,s^{-1}$, the differential stress calculated for sheared myrmekite deforming via diffusion creep is <45 MPa. Under the constant strain rate assumption, the strength contrast between monomineralic Qtz and sheared myrmekite is not quantifiable; however, the sheared myrmekite are always weaker than monomineralic Qtz deforming via dislocation creep. Strain rates of the order of 10^{-11}–$10^{-13}\,s^{-1}$ would require grain sizes in the range of 10–100 µm in the sheared myrmekite deforming by diffusion creep only (grey shaded areas in Fig. 9b).

Figure 9d shows the different curves describing the rheological behaviour of a simplified granitoid rock where Kfs is progressively replaced, up to 20 % vol, by sheared

myrmekite. The flow behaviour of the derived granitoid mylonite is represented by the grey curves, and is linear viscous for most of the investigated conditions. The complete consumption of Kfs results in 3–4 orders of magnitude increase in strain rate at differential stress conditions of 70 MPa (inset of Fig. 9d), consistent with experimental observations (Xiao et al., 2002). A similar increase in strain rate is already observed for a 5 % vol of sheared myrmekite in the total rock volume. These results can be compared to the different degree of myrmekite substitution observed along the strain gradient in the shear zone and also could explain the progressive increase in strain toward the ultramylonite with increasing myrmekite substitution (Fig. 2), suggesting positive feedback between strain-induced myrmekite formation and strain accommodation. Dissolution–precipitation creep of Kfs and associated GSS creep in Kfs + Plg + Qtz aggregates have been already described by Behrmann and Mainprice (1987) as an efficient strain accommodation and weakening mechanism in Qtz–feldspar mylonites. In the Rieserferner mylonites, GSS creep of Kfs seems to be dominant in protomylonite, but its role decreases with increasing myrmekite substitution (Fig. 2). The positive correlation between accommodated strain and amount of sheared myrmekite suggests that GSS creep processes in Kfs are not capable of accommodating strain at rates comparable to those produced by GSS creep in sheared myrmekite.

The effect of myrmekite development in rheological weakening might be overestimated by our calculation for two main reasons: (i) other weakening mechanisms, which are not considered in our simplified model of granitoid (such as feldspar GSS creep, Bt deformation), may have concurred with deformation; and (ii) at low strain, myrmekite aggregates were initially non-interconnected pockets (e.g. Handy, 1994). Strain weakening associated with myrmekite is inferred to become relevant as, with increasing strain and volume fraction of sheared myrmekite, the initially isolated myrmekite are sheared and coalesced into an interconnected network. In the Rieserferner sheared granodiorites, an interconnected framework of sheared myrmekite is established in the presence of 5 % vol to 7 % vol of myrmekite and is well developed at 10 % vol–15 % vol (Fig. 2). Therefore, mylonites containing up to 15 % vol of sheared myrmekite ideally underwent deformation at strain rates of 10^{-10}–10^{-11} s^{-1} and at differential stresses in the range between 10 and 70 MPa (transparent red area bracketed by the curves calculated for 10 % vol and 20% vol of myrmekite substitution in Fig. 9d). These mylonites were synkinematic to mylonitic Qtz veins described in Ceccato et al. (2017), for which Qtz paleopiezometry retrieved comparable strain rates of 10^{-11} s^{-1} for 117 MPa differential stress.

9 Conclusions

Metamorphic reactions contributed importantly to strain weakening within the Rieserferner granitoid mylonites. A primary grain-size reduction mechanism was related to the development of myrmekite evolving, with increasing strain, to weak aggregates of Qtz and Plg. Topotactic replacement has been inferred from the coincidence between myrmekitic Plg and parent Kfs grain crystal lattices in pristine myrmekite. Transition from pristine myrmekite to fine-grained sheared myrmekite involved microfracturing, annealing, and shearing of the resulting granoblastic aggregate. Sheared myrmekite consists of fine-grained Plg + Qtz aggregates (7 and 4 µm in grain size, respectively) that show anti-clustered spatial distribution and well-defined SPO; Qtz usually occurs at triple and quadruple junctions between Plg grains. Both Plg and Qtz show weak CPOs and almost uniform misorientation angle distributions. The microstructures of sheared myrmekite suggest that different deformation mechanisms occurred in Plg and Qtz: Plg mainly deformed by GSS creep, whereas dissolution–precipitation and nucleation processes were dominant in Qtz. Myrmekite formation also promoted phase mixing, as the pristine myrmekite microstructure predisposed the development of an "anti-clustered" spatial distribution of phases in the recrystallized aggregate. Strong grain-size reduction and the nucleation of Plg + Qtz polymineralic aggregates led to a switch in the dominant deformation mechanisms, activating GSS creep processes and triggered phase mixing. GSS processes and phase mixing inhibited grain growth and stabilized grain size, hindering the efficiency of dynamic recrystallization by dislocation creep processes and self-sustaining the activity of GSS processes. Therefore, the formation of myrmekite led to the activation of self-sustaining weakening processes. Results of rheological calculations show that, at the conditions of Rieserferner mylonitization, sheared myrmekite are several orders of magnitude weaker than both pure Qtz layers and ideal granitoid rock deforming via dislocation creep. Strain-rate partitioning is therefore expected to occur between sheared myrmekite and monomineralic Qtz layers, and the occurrence of ca. 5 % vol of myrmekite could lead to an increase of 3–4 orders of magnitude in strain rate. However, the effective role of myrmekite in rock weakening depends on the evolution of the rock microstructure. Effective weakening requires interconnection of sheared myrmekite layers, which occurs after the development of 10 % vol–15 % vol of myrmekite. This work highlights the importance of metamorphic reactions as grain-size reduction mechanisms in feldspar, and their role in localization of ductile deformation via the activation of GSS creep. The microstructural results and the rheological calculation presented here will be useful for further development of detailed rheological models of feldspar-rich rocks at mid-crustal conditions.

Code and data availability. The MATLAB script used for rheological calculation is available on request from the first author. Supplementary data are available in the Supplement.

Appendix A: Methods

A1 EBSD sample preparation and data processing

The thin section was SYTON-polished for ca. 3 h and carbon coated. All data have been processed and analysed using CHANNEL5 software of HKL Technology, Oxford Instruments. Noise reduction was applied following Bestmann and Prior (2003). Local mis-indexing between Plg and Kfs was resolved by nullifying the subset of selected grains with area $< 1\,\mu m^2$ in each map. Dauphiné twins smaller than 0.5 µm have been interpreted as an error from mis-indexing and were replaced by the average orientation of the neighbouring pixels. The indexed phases and relative symmetry group used for the indexing are quartz – trigonal -3m; plagioclase (anorthite) – triclinic -1; and orthoclase – monoclinic 2/m. Critical misorientation for the distinction between low- and high-angle boundaries have been chosen at 10°. Qtz grain boundaries with $60° \pm 5°$ of misorientation were disregarded from the grain detection procedure to avoid any contribution from Dauphiné twinning. Plg grain boundaries with $180° \pm 5°$ of misorientation around [010] were disregarded from the grain detection procedure to avoid any contribution from Albite twinning. The pole figures (one point per grain, where not differently specified) are plotted as equal area, lower hemisphere projections oriented with the general shear zone kinematics reference system ($X =$ stretching lineation; $Z =$ pole to general shear plane/vein boundary); whereas the misorientation axis distributions in sample coordinates are plotted as equal area, upper hemisphere projections. The inverse pole figures for misorientation axis distribution in crystal coordinates are upper hemisphere projections. Contoured projections have constant contouring parameters (halfwidth: 10°). Contouring lines are given only for the 0.5–10 m.u.d. (multiple of uniform distributions) range.

A2 Grain size analysis

Grain sizes were obtained from the grain detection routine of the HKL Channel5 Tango software. The grain size was calculated as diameter of the circle with an equivalent area. The minimum cut-off area was set to $1\,\mu m^2$, which means that only grains of a size ≥ 4 or ≥ 9 pixels (depending on the map acquisition step size) were considered. Grain size data were represented as area-weighted distributions by plotting frequency against the square-root grain-size-equivalent grain diameters (as in Herwegh and Berger, 2004; Berger et al., 2011). The grain size distribution approaches a Gaussian distribution when plotted in this way, allowing a good estimate of the mean grain size. The geometric mean grain size (red thick line in grain size distribution diagrams) was obtained graphically as the maximum frequency grain size of the distribution curve.

A3 Image analysis

Image analysis of grain shape was performed on both scanning electron microscope backscattered electron (SEM-BSE) images and phase maps obtained from EBSD. Quantification of phase amount (% vol) was performed through segmentation of SEM-BSE images of a whole thin section collected at the Electron Microscopy Centre of the University of Plymouth. Image processing and thresholding was done with the ImageJ software, and further processing together with manual correction were applied to improve data quality and to ensure the correspondence of greyscale ranges with specific mineral phases. Grain boundary images and phase distribution images were obtained directly from EBSD phase maps and grain boundary maps elaborated by Channel5 (HKL Technology). Before the analysis with ImageJ software, images were manually corrected in order to exclude mis-indexing and non-indexed orientation pixels. Grain boundaries and phase amount have been quantified by pixel counting.

Supplement. The supplement related to this article is available online at: https://doi.org/10.5194/se-9-1399-2018-supplement.

Author contributions. AC, LM and GP developed the initial idea of the study and performed the initial exploratory SEM study. GP collected the samples of Rieserferner mylonites. LM acquired EBSD data. AC performed EBSD data processing and analysis, and the rheological calculations. LFGM performed cathodoluminescence analysis. AC prepared the figures and the manuscript with contributions from all the co-authors.

Competing interests. The authors declare that they have no conflict of interest.

Acknowledgements. Elena A. Miranda, James Gilgannon, the topical editor Florian Fusseis, and three anonymous reviewers are warmly thanked for their comments and reviews. Simone Papa, Francesco Giuntoli, and Luca Pellegrino are thanked for fruitful discussions. Andrea Risplendente is thanked for his help during EMPA data collection at the Università degli Studi di Milano. The staff at the University of Plymouth Electron Microscopy Centre is thanked for the assistance during EBSD data acquisition. Luca Menegon acknowledges the financial support from a FP7 Marie Curie Career Integration Grant (grant agreement PCIG13-GA-2013-618289). Financial support from the University of Padova ("Progetto di Ateneo" CPDA140255) and from the Foundation "Ing. Aldo Gini" is acknowledged.

Edited by: Florian Fusseis
Reviewed by: Elena A. Miranda, Takamoto Okudaira, James Gilgannon, and one anonymous referee

References

Abart, R., Heuser, D., and Habler, G.: Mechanisms of myrmekite formation: case study from the Weinsberg granite, Moldanubian zone, Upper Austria, Contrib. Mineral. Petr., 168, 1074 https://doi.org/10.1007/s00410-014-1074-7, 2014.

Becke, F.: Über myrmekite, Mineralogie und Pétrographie Mitteilungen 27, 377–390, 1908.

Behrmann, J. H. and Mainprice, D.: Deformation mechanisms in a high-temperature quartz-feldspar mylonite: evidence for superplastic flow in the lower continental crust, Tectonophysics, 140, 297–305, 1987.

Bellieni, G.: Caratteri geochimici del massiccio granodioritico tonalitico delle Vedrette di Ries (Rieserferner) – Alto Adige Orientale, Rendiconti della Società Italiana di Mineralogia e Petrologia 34, 527–548, 1978.

Berger, A., Herwegh, M., Schwarz, J. O., and Putlitz, B.: Quantitative analysis of crystal/grain sizes and their distributions in 2D and 3D, J. Struct. Geol., 33, 1751–1763, 2011.

Bestmann, M. and Pennacchioni, G.: Ti distribution in quartz across a heterogeneous shear zone within a granodiorite: The effect of deformation mechanism and strain on Ti resetting, Lithos, 227, 37–56, 2015.

Bestmann, M. and Prior, D. J.: Intragranular dynamic recrystallization in naturally deformed calcite marble: diffusion accommodated grain boundary sliding as a result of subgrain rotation recrystallization, J. Struct. Geol., 25, 1597–1613, 2003.

Boullier, A. M. and Gueguen, Y.: SP-mylonites: origin of some mylonites by superplastic flow, Contrib. Mineral. Petr., 50, 93–104, 1975.

Burnham, C. W., Holloway, J. R., and Davis, N. F.: Thermodynamic Properties of Water to 1000 °C and 10,000 Bars, Geol. Soc. Am. Bull., 132, 1–96, https://doi.org/10.1130/SPE132, 1969.

Ceccato, A.: Structural evolution of Periadriatic plutons and its implications on solid-state deformation of granitoid rocks. Università degli Studi di Padova, PhD Thesis, pp. 250, 2018.

Ceccato, A. and Pennacchioni, G.: Structural evolution of the Rieserferner Pluton in the framework of the Tertiary tectonics of the Eastern Alps, J. Struct. Geol., 116, 64–80, https://doi.org/10.1016/j.jsg.2018.08.004, 2018.

Ceccato, A., Pennacchioni, G., Menegon, L., and Bestmann, M.: Crystallographic control and texture inheritance during mylonitization of coarse grained quartz veins, Lithos 290–291, 210–227, https://doi.org/10.1016/j.lithos.2017.08.005, 2017.

Cesare, B., Marchesi, C., and Connolly, J.A.D.: Growth of myrmekite coronas by contact metamorphism of granitic mylonites in the aureole of Cima di Vila, Eastern Alps, Italy, J. Metamorph. Geol., 20, 203–213, 2002.

Cesare, B., Mazzoli, C., Sassi, R., Spiess, R., and Sassi, F. P.: Beauty and complexity of metamorphism: case studies from the frontal part of the Adria microplate, Rend. Lincei, 21, 73–94, 2010.

Ciancaleoni, L. and Marquer, D.: Syn-extension leucogranite deformation during convergence in the Eastern Central Alps: example of the Novate intrusion, Terra Nova, 18, 170–180, 2006.

Cross, A. J., Prior, D. J., Stipp, M., and Kidder, S.: The recrystallized grain size piezometer for quartz: An EBSD-based calibration, Geophys. Res. Lett., 44, 6667–6674, 2017.

Czaplińska, D., Piazolo, S., and Zibra, I.: The influence of phase and grain size distribution on the dynamics of strain localization in polymineralic rocks, J. Struct. Geol., 72, 15–32 2015.

De Toni, G. B., Bitencourt, M. F., and Nardi, L. V. S.: Strain partitioning into dry and wet zones and the formation of Ca-rich myrmekite in syntectonic syenites: A case for melt-assisted dissolution-replacement creep under granulite facies conditions, J. Struct. Geol., 91, 88–101, 2016.

Dégi, J., Abart, R., Török, K., Bali, E., Wirth, R., and Rhede, D.: Symplectite formation during decompression induced garnet breakdown in lower crustal mafic granulite xenoliths: mechanisms and rates, Contrib. Mineral. Petr., 159, 293–314, 2010.

Dell'Angelo, L. N. and Tullis, J.: Textural and mechanical evolution with progressive strain in experimentally deformed aplite, Tectonophysics, 256, 57–82, 1996.

Den Brok, S. W. J.: Effect of microcracking on pressure-solution strain rate: The Gratz grain-boundary model, Geology, 26, 915–918, 1998.

Dimanov, A. and Dresen, G.: Rheology of synthetic anorthite-diopside aggregates: Implications for ductile shear zones, J. Geophys. Res.-Sol. Ea., 110, 1–24, https://doi.org/10.1029/2004JB003431, 2005.

Fliervoet, T. F., White, S. H., and Drury, M. R.: Evidence for dominant grain-boundary sliding deformation in greenschist-and amphibolite-grade polymineralic ultramylonites from the Red-

bank Deformed Zone, Central Australia, J. Struct. Geol., 19, 1495–1520, 1997.

Fournier, R. O. and Potter II, R. W.: An equation correlating the solubility of quartz in water from 25 to 900 °C at pressures up to 10 000 bars, Geochim. Cosmochim. Ac., 46, 1969–1973, 1982.

Fusseis, F., Regenauer-Lieb, K., Liu, J., Hough, R. M., and De Carlo, F.: Creep cavitation can establish a dynamic granular fluid pump in ductile shear zones, Nature 459, 974–977, https://doi.org/10.1038/nature08051, 2009.

Götze, J., Habermann, D., Neuser, R. D., and Richter, D. K.: High-resolution spectrometric analysis of rare earth elements-activated cathodoluminescence in feldspar minerals, Chem. Geol., 153, 81–91, 1999.

Gueydan, F., Leroy, Y. M., Jolivet, L., and Agard, P.: Analysis of continental midcrustal strain localization induced by microfracturing and reaction-softening, J. Geophys. Res.-Sol. Ea., 108, 2064, https://doi.org/10.1029/2001JB000611, 2003.

Handy, M. R.: The solid-state flow of polymineralic rocks, J. Geophys. Res.-Sol. Ea., 95, 8647–8661, 1990.

Handy, M. R.: Flow laws for rocks containing two non-linear viscous phases: a phenomenological approach, J. Struct. Geol., 16, 287–301, 1994.

Heilbronner, R. and Barrett, S.: Image Analysis in Earth Sciences, pp. 520, Springer, Berlin, Heidelberg, 2014.

Herwegh, M. and Berger, A.: Deformation mechanisms in second-phase affected microstructures and their energy balance, J. Struct. Geol., 26, 1483–1498, 2004.

Herwegh, M., Linckens, J., Ebert, A., Berger, A., and Brodhag, S. H.: The role of second phases for controlling microstructural evolution in polymineralic rocks: A review, J. Struct. Geol., 33, 1728–1750, 2011.

Hiraga, T., Miyazaki, T., Yoshida, H., and Zimmerman, M. E.: Comparison of microstructures in superplastically deformed synthetic materials and natural mylonites: Mineral aggregation via grain boundary sliding, Geology, 41, 959–962, 2013.

Hirth, G., Teyssier, C., and Dunlap, J. W.: An evaluation of quartzite flow laws based on comparisons between experimentally and naturally deformed rocks, Int. J. Earth Sci., 90, 77–87, 2001.

Hopson, R. F. and Ramseyer, K.: Cathodoluminescence microscopy of myrmekite, Geology, 18, 336–339, 1990.

Jiang, Z., Prior, D. J., and Wheeler, J.: Albite crystallographic preferred orientation and grain misorientation distribution in a low-grade mylonite: implications for granular flow, J. Struct. Geol., 22, 1663–1674, 2000.

Johnson, S. E., Marsh, J. H., and Vernon, R. H.: From tonalite to mylonite: coupled mechanical and chemical processes in foliation development and strain localization, Journal of Virtual Explorer, 30, https://doi.org/10.3809/jvirtex.2009.00208, 2008.

Kilian, R., Heilbronner, R., and Stünitz, H.: Quartz grain size reduction in a granitoid rock and the transition from dislocation to diffusion creep, J. Struct. Geol., 33, 1265–1284, 2011.

Kruse, R. and Stünitz, H.: Deformation mechanisms and phase distribution in mafic high-temperature mylonites from the Jotun Nappe, southern Norway, Tectonophysics, 303, 223–249, 1999.

Kruse, R., Stünitz, H., and Kunze, K.: Dynamic recrystallization processes in plagioclase porphyroclasts, J. Struct. Geol., 23, 1781–1802, 2001.

Lapworth, T., Wheeler, J., and Prior, D. J.: The deformation of plagioclase investigated using electron backscatter diffraction crystallographic preferred orientation data, J. Struct. Geol., 24, 387–399, 2002.

LaTour, T. E. and Barnett, R. L.: Mineralogical changes accompanying mylonitization in the Bitterroot dome of the Idaho batholith: Implications for timing of deformation, Geol. Soc. Am. Bull., 98, 356–363, 1987.

McCaffrey, K. J.: Magmatic and solid state deformation partitioning in the Ox Mountains Granodiorite, Geol. Mag., 131, 639–652, 1994.

Menegon, L. and Pennacchioni, G.: Local shear zone pattern and bulk deformation in the Gran Paradiso metagranite (NW Italian Alps), Int. J. Earth Sci., 99, 1805–1825, https://doi.org/10.1007/s00531-009-0485-6, 2010.

Menegon, L., Pennacchioni, G., and Stünitz, H.: Nucleation and growth of myrmekite during ductile shear deformation in metagranites, J. Metamorph. Geol., 24, 553–568, 2006.

Menegon, L., Pennacchioni, G., and Spiess, R.: Dissolution-precipitation creep of K-feldspar in mid-crustal granite mylonites, J. Struct. Geol., 30, 565–579, 2008.

Menegon, L., Stünitz, H., Nasipuri, P., Heilbronner, R., and Svahnberg, H.: Transition from fracturing to viscous flow in granulite facies perthitic feldspar (Lofoten, Norway), J. Struct. Geol., 48, 95–112, 2013.

Menegon, L., Fusseis, F., Stünitz, H., and Xiao, X.: Creep cavitation bands control porosity and fluid flow in lower crustal shear zones, Geology, 43, 227–230, 2015.

Michibayashi, K.: The role of intragranular fracturing on grain size reduction in feldspar during mylonitization, J. Struct. Geol., 18, 17–25, 1996.

Miranda, E. A., Hirth, G., and John, B. E.: Microstructural evidence for the transition from dislocation creep to dislocation-accommodated grain boundary sliding in naturally deformed plagioclase, J. Struct. Geol., 92, 30–45, 2016.

O'Hara, K. D., Sharp, Z. D., Moecher, D. P., and Jenkin, G. T.: The effect of deformation on oxygen isotope exchange in quartz and feldspar and the significance of isotopic temperatures in mylonites, J. Geol., 105, 193–204, 1997.

Odashima, N., Morishita, T., Ozawa, K., Nagahara, H., Tsuchiyama, A., and Nagashima, R.: Formation and deformation mechanisms of pyroxene-spinel symplectite in an ascending mantle, the Horoman peridotite complex, Japan: An EBSD (electron backscatter diffraction) study, J. Miner. Petrol. Sci., 103, 1–15, 2007.

Okudaira, T. and Shigematsu, N.: Estimates of stress and strain rate in mylonites based on the boundary between the fields of grain-size sensitive and insensitive creep, J. Geophys. Res.-Sol. Ea., 117, B03210, https://doi.org/10.1029/2011JB008799, 2012.

Pennacchioni, G.: Control of the geometry of precursor brittle structures on the type of ductile shear zone in the Adamello tonalites, Southern Alps (Italy), J. Struct. Geol., 27, 627–644, 2005.

Pennacchioni, G. and Mancktelow, N. S.: Nucleation and initial growth of a shear zone network within compositionally and structurally heterogeneous granitoids under amphibolite facies conditions, J. Struct. Geol., 29, 1757–1780, 2007.

Pennacchioni, G. and Mancktelow, N. S.: Small-scale ductile shear zones: neither extending, nor thickening, nor narrowing, Earth-Sci. Rev., 184, 1–12, https://doi.org/10.1016/j.earscirev.2018.06.004, 2018.

Pennacchioni, G. and Zucchi, E.: High temperature fracturing and ductile deformation during cooling of a pluton: The Lake Edison granodiorite (Sierra Nevada batholith, California), J. Struct. Geol., 50, 54–81, 2013.

Pennacchioni, G., Di Toro, G., Brack, P., Menegon, L., and Villa, I. M.: Brittle–ductile–brittle deformation during cooling of tonalite (Adamello, Southern Italian Alps), Tectonophysics, 427, 171–197, 2006.

Pennacchioni, G., Menegon, L., Leiss, B., Nestola, F., and Bromiley, G.: Development of crystallographic preferred orientation and microstructure during plastic deformation of natural coarse-grained quartz veins, J. Geophys. Res.-Sol. Ea., 115, B12405, https://doi.org/10.1029/2010JB007674, 2010.

Phillips, E. R.: On polygenetic myrmekite, Geol. Mag., 117, 29–36, 1980.

Pitzer, K. S. and Sterner, S. M.: Equations of state valid continuously from zero to extreme pressures for H_2O and CO_2, J. Chem. Phys., 101, 3111–3116, 1994.

Platt, J. P.: Rheology of two-phase systems: A microphysical and observational approach, J. Struct. Geol., 77, 213–227, 2015.

Ramseyer, K., AlDahan, A. A., Collini, B., and Landström, O.: Petrological modifications in granitic rocks from the Siljan impact structure: evidence from cathodoluminescence, Tectonophysics, 216, 195–204, 1992.

Ree, J. H., Kim, H. S., Han, R., and Jung, H.: Grain-size reduction of feldspars by fracturing and neocrystallization in a low-grade granitic mylonite and its rheological effect, Tectonophysics, 407, 227–237, 2005.

Romer, R. L. and Siegesmund, S.: Why allanite may swindle about its true age, Contrib. Mineral. Petr., 146, 297–307, 2003.

Rybacki, E. and Dresen, G.: Deformation mechanism maps for feldspar rocks, Tectonophysics, 382, 173–187, 2004.

Rybacki, E., Gottschalk, M., Wirth, R., and Dresen, G.: Influence of water fugacity and activation volume on the flow properties of fine-grained anorthite aggregates, J. Geophys. Res.-Sol. Ea., 111, B03203, https://doi.org/10.1029/2005JB003663, 2006.

Shimamoto, T., Kanaori, Y., and Asai, K. I.: Cathodoluminescence observations on low-temperature mylonites: potential for detection of solution-precipitation microstructures, J. Struct. Geol., 13, 967–973, 1991.

Simpson, C. and Wintsch, R. P.: Evidence for deformation-induced K-feldspar replacement by myrmekite, J. Metamorph. Geol., 7, 261–275, 1989.

Słaby, E., Götze, J., Wörner, G., Simon, K., Wrzalik, R., and Śmigielski, M.: K-feldspar phenocrysts in microgranular magmatic enclaves: a cathodoluminescence and geochemical study of crystal growth as a marker of magma mingling dynamics, Lithos, 105, 85–97, 2008.

Słaby, E., Domonik, A., Śmigielski, M., Majzner, K., Motuza, G., Götze, J., and Rydelek, P.: Protomylonite evolution potentially revealed by the 3D depiction and fractal analysis of chemical data from a feldspar, Contrib. Mineral. Petr., 167, 995, https://doi.org/10.1007/s00410-014-0995-5, 2014.

Stel, H. and Breedveld, M.: Crystallographic orientation patterns of myrmekitic quartz: a fabric memory in quartz ribbon-bearing gneisses, J. Struct. Geol., 12, 19–28, 1990.

Stipp, M. and Tullis, J.: The recrystallized grain size piezometer for quartz, Geophys. Res. Lett., 30, 2088, https://doi.org/10.1029/2003GL018444, 2003.

Stipp, M., Stünitz, H., Heilbronner, R., and Schmid, S. M.: The eastern Tonale fault zone: a "natural laboratory" for crystal plastic deformation of quartz over a temperature range from 250 to 700 °C, J. Struct. Geol., 24, 1861–1884, 2002.

Stipp, M., Tullis, J., Scherwath, M., and Behrmann, J. H.: A new perspective on paleopiezometry: Dynamically recrystallized grain size distributions indicate mechanism changes, Geology, 38, 759–762, 2010.

Stünitz, H. and Fitz Gerald, J. F.: Deformation of granitoids at low metamorphic grade. II: Granular flow in albite-rich mylonites, Tectonophysics, 221, 299–324, 1993.

Stünitz, H. and Tullis, J.: Weakening and strain localization produced by syn-deformational reaction of plagioclase, Int. J. Earth Sci., 90, 136–148, 2001.

Tsurumi, J., Hosonuma, H., and Kanagawa, K.: Strain localization due to a positive feedback of deformation and myrmekite-forming reaction in granite and aplite mylonites along the Hatagawa Shear Zone of NE Japan, J. Struct. Geol., 25, 557–574, 2003.

Vernon, R. H.: Questions about myrmekite in deformed rocks, J. Struct. Geol., 13, 979–985, 1991.

Viegas, G., Menegon, L., and Archanjo, C.: Brittle grain-size reduction of feldspar, phase mixing and strain localization in granitoids at mid-crustal conditions (Pernambuco shear zone, NE Brazil), Solid Earth, 7, 375–396, https://doi.org/10.5194/se-7-375-2016, 2016.

Wheeler, J., Prior, D., Jiang, Z., Spiess, R., and Trimby, P.: The petrological significance of misorientations between grains, Contrib. Mineral. Petr., 141, 109–124, 2001.

White, S.: Geological significance of recovery and recrystallization processes in quartz, Tectonophysics, 39, 143–170, 1977.

Wirth, R. and Voll, G.: Cellular intergrowth between quartz and sodium-rich plagioclase (myrmekite) – an analogue of discontinuous precipitation in metal alloys, J. Mater. Sci., 22, 1913–1918, 1987.

Xiao, X., Wirth, R., and Dresen, G.: Diffusion creep of anorthite-quartz aggregates, J. Geophys. Res.-Sol. Ea., 107, 2279, https://doi.org/10.1029/2001JB000789, 2002.